

AD/A-001 061

A SOURCE THEORY FOR COMPLEX EARTHQUAKES

R. R. Blandford

Teledyne Geotech

Prepared for:

Defense Advanced Research Projects Agency
VELA Seismological Center

10 April 1974

DISTRIBUTED BY:

NTIS

National Technical Information Service
U. S. DEPARTMENT OF COMMERCE

SECURITY CLASSIFICATION OF THIS PAGE (When Data Entered)

DD FORM 1473 EDITION OF 1 NOV 65 IS OBSOLETE

Unclassified
SECURITY CLASSIFICATION OF THIS PAGE (When Data Entered)

Unclassified

SECURITY CLASSIFICATION OF THIS PAGE(When Data Entered)

- P corner frequency higher than S corner frequency;
- High-frequency P/S amplitude ratio higher than previous theories predict;
- Increase of complexity as a function of third moment;
- Small m_b relative to M_s for transform faults.

The theory predicts that $M_s:m_b$ populations of earthquakes and explosions will not converge at small magnitudes.

Unclassified

SECURITY CLASSIFICATION OF THIS PAGE(When Data Entered)

A SOURCE THEORY FOR COMPLEX EARTHQUAKES

SEISMIC DATA ANALYSIS CENTER REPORT NO.: SDAC-TR-74-4

AFTAC Project No.: VELA VT/4709
Project Title: Seismic Data Analysis Center
ARPA Order No.: 1620
ARPA Program Code No.: 3F10

Name of Contractor: TELEDYNE GEOTECH

Contract No.: F08606-74-C-0006
Date of Contract: 01 July 1973
Amount of Contract: \$2,152,172
Contract Expiration Date: 30 June 1974
Project Manager: Royal A. Hartenberger
(703) 836-3882

P. O. Box 334, Alexandria, Virginia 22314

APPROVED FOR PUBLIC RELEASE; DISTRIBUTION UNLIMITED.

ABSTRACT

Earthquake source theories of Haskell, Brune, and Savage have been drawn upon to develop a description of an earthquake as a major slip accompanied by many smaller tensional and slip events. We find natural explanations of several previously unexplained observations, such as:

- Robustness of the $M_s:m_b$ discriminant,
- P corner frequency higher than S corner frequency
- High-frequency P/S amplitude ratio higher than previous theories predict,
- Increase of complexity as a function of third moment,
- Small m_b relative to M_s for transform faults.

The theory predicts that $M_s:m_b$ populations of earthquakes and explosions will not converge at small magnitudes.

TABLE OF CONTENTS

	<u>Page</u>
ABSTRACT	
INTRODUCTION	1
THEORY	12
THEORETICAL RESULTS	24
COMPARISON WITH OBSERVATION	34
SUMMARY AND SUGGESTIONS FOR FURTHER RESEARCH	41
REFERENCES	44

LIST OF TABLES

Table No.	Title	Page
1	Earthquake Parameters Fixed in this Report	25
2	Earthquake Parameters for Earthquakes Plotted in Figure 30. From Douglas et al. (1973).	35

LIST OF FIGURES

Figure No.	Title	Page
1	B functions for a slip earthquake with slip in direction of fault propagation. Curves are the same as those plotted by Haskell (1964).	52
2	B functions for all three types of fault motion considered by Haskell (1964). Plotted from formulas given by Haskell.	53
3	Variations in amplitude as a function of propagation velocity for the B functions for a slip earthquake with slip in direction of fault propagation. Intermediate slope of ω^{-1} can be seen at high velocities for the shear (B_2) functions.	54
4	Variations in amplitude as a function of propagation velocity for the B functions for a slip earthquake with slip in fault plane and perpendicular to direction of fault propagation. Intermediate slope is not so apparent as in Figure 3.	55
5	Variations in amplitude as a function of propagation velocity for the B functions for a tensional earthquake. Intermediate slope is not so apparent as in Figure 3.	56
6	S and P displacement amplitude spectra and their ratio for a simple earthquake.	57
7	S and P displacement amplitude spectra and their ratio for a simple earthquake, plus one sublevel.	58

LIST OF FIGURES (Continued)

Figure No.	Title	Page
8	S and P displacement amplitude spectra and their ratio for three simple earthquakes of different sizes. Note the convergence of amplitude at high frequencies; and the "periodic" behavior of the ratios.	59
9	S and P displacement amplitude spectra and their ratio for three types of simple earthquakes.	60
10	S and P displacement amplitude spectra and their ratio for three types of simple earthquakes, plus one sublevel.	61
11	S and P displacement amplitude spectra and their ratio for a simple earthquake plus 0, 1, 2, 3, or 4 sublevels.	62
12	S and P displacement amplitude spectra and their ratio for a simple earthquake plus one sublevel with a range of submoments.	63
13	S and P displacement amplitude spectra and their ratio for a simple earthquake plus one sublevel with a range of earthquake sizes but constant total moment.	64
14	S and P displacement amplitude spectra and their ratio for a simple earthquake and with a range of propagation velocities.	65
15	S and P displacement amplitude spectra and their ratio for a simple earthquake plus one sublevel, for a range of propagation velocities.	66

LIST OF FIGURES (Continued)

Figure No.	Title	Page
16	S and P displacement amplitude spectra and their ratio for a simple earthquake and with a range of fractional stress drops. An intermediate slope of ω^{-1} can be seen.	67
17	S and P displacement amplitude spectra and their ratio for a simple earthquake plus one sublevel for a range of fractional stress drops.	68
18	20-second total displacement versus 1-second compressional displacement for simple earthquakes for a range of lengths.	69
19	20-second total displacement versus 1-second compressional displacement for simple earthquakes for a range of lengths plus 0, 2, 4, or 6 sublevels with constant total moment leading to an increase of 25%. Ratio of subearthquake lengths $r = 0.33$.	70
20	20-second total displacement versus 1-second compressional displacement for simple earthquakes for a range of lengths, plus 0, 2, 4, or 6 sublevels with constant total moment leading to an increase of 1%. Ratio of subearthquake lengths $r = 0.33$.	71
21	20-second total displacement versus 1-second compressional displacement for simple earthquakes for a range of lengths plus 0, 2, 4, or 6 sublevels with constant total moment leading to an increase of 25%. Ratio of subearthquake lengths $r = 0.57$.	72

LIST OF FIGURES (Continued)

Figure No.	Title	Page
22	20-second total displacement versus 1-second compressional displacement for simple earthquakes for a range of lengths, plus 0, 2, 4, or 6 sublevels with constant total moment leading to an increase of 1%. Ratio of subearthquake lengths $r = 0.57$.	73
23	20-second total displacement versus 1-second compressional displacement for simple earthquakes for a range of lengths, plus 4 sublevels with constant total moment leading to an increase of 1%. A range of fractional stress drops is presented, successive points are connected by dashed lines.	74
24	20-second total displacement versus 1-second compressional displacement for simple earthquakes for a range of lengths, plus 4 sublevels with constant total moment leading to an increase of 1%. A range of propagation velocities is seen to affect the plot substantially less than does a range of subearthquake levels.	75
25	20-second total displacement versus 1-second compressional displacement for simple earthquakes for a range of lengths, plus 4 sublevels with constant total moment leading to an increase of 1%. The effects of a range in fractional stress drop and propagation velocity can be seen.	76

LIST OF FIGURES (Continued)

Figure No.	Title	Page
26	20-second total displacement versus 1-second compressional displacement for simple earthquakes for a range of lengths, plus 4 sublevels with constant total moment leading to an increase of 1%. The effects of variation in the type of the simple earthquake can be seen to be relatively minor except for earthquakes already near the limiting line.	77
27	Displacement amplitude spectra for explosions in granite using the data of Werth and Herbst (1963) and the formulas of von Seggern and Blandford (1972).	78
28	20-second displacement versus 1-second displacement for explosions in granite using the data of Werth and Herbst (1963) and the formulas of von Seggern and Blandford (1973), for a range of yields.	79
29	20-second displacement versus 1-second displacement for explosions in granite using the data of Werth and Herbst (1963) and the formulas of von Seggern and Blandford (1973), for a range of yields. Figure has been calibrated to M_s and m_b values by use of solution for 100 kt explosion given by Douglas et al. (1973). Limiting earthquake line has also been drawn in.	80
30	$M_s:m_b$ plot from Douglas et al. (1973) (see Table 2), together with the granite explosion line from Figure 29, and the limiting earthquake line.	81

LIST OF FIGURES (Continued)

Figure No.	Title	Page
31	$M_S:m_b$ for U.S. earthquakes and explosions. Open symbols are earthquakes, closed symbols are explosions. From Evernden et al. (1971). Granite explosion line and limiting earthquake line have been drawn onto the original figure.	81
32a-h	Pacoima Dam accelerograms of San Fernando aftershocks.	82
33	Fourier amplitude spectra of ground acceleration at the Pacoima Dam site for 13 aftershocks. From Trifunac (1972). The dots are the calculated and corrected average spectra. Full lines are Trifunac's theoretical spectra.	85
34	P-wave corner frequencies versus S-wave corner frequencies for large aftershocks of the 1971 San Fernando earthquake by the strong-motion instrument at Pacoima Dam. From Molnar et al. (1973) using data from Trifunac (1972).	86
35	P-wave corner frequencies versus S-wave corner frequencies for earthquakes studies by Molnar et al. (1973).	87
36	Average third moment of frequency against complexity for a population of twenty-seven Eurasian explosions (solid dots) and fifty-one shallow Eurasian earthquakes (open circles). From Anglin (1971).	88

INTRODUCTION

Haskell (1964) developed a theory for the spectral distribution of the teleseismic compressional and shear radiation from long thin strike-slip or tensional earthquakes in a homogeneous infinite elastic space. He noted that the strike-slip earthquakes had a higher S/P (shear-to-compressional) energy ratio than was commonly observed, and speculated that most earthquakes have a small component of tensional faulting. He suggested that since tensional faults have a lower S/P ratio than do strike-slip earthquakes, a small portion of tensional cracking could dramatically alter the S/P ratio. Haskell also had some difficulty in matching the existing evidence on the ratio of short-period to long-period energy, and speculated that the fault surface might be "rough". This possibility he modeled in two ways: first, by allowing the ramp displacement function to be modulated by a sine wave, and second, by assuming that for high frequencies the fault acts as the sum of several small faults. Haskell's (1969) paper developed techniques for calculating the near-field displacement from slip or tensional earthquakes.

In Haskell (1966) he extended the idea of a modulated ramp displacement function to a stochastic displacement function. The ensemble of displacement functions was characterized by the average autocorrelation of the ensemble. This average autocorrelation led then to an average spectrum. Haskell chose the

autocorrelation function to be similar to that of the sine-wave modulated ramp function in his 1964 paper, except that it had no periodic factor, and satisfied an integral constraint resulting from the fact that the earthquake must begin and end in a state of static equilibrium.

The displacement spectrum resulting from this autocorrelation behaved at high frequencies like ω^{-3} (the spectrum resulting from the modulated ramp function was asymptotic as ω^{-4}). Aki (1967) showed that an ω^{-3} asymptote leads to predictions for the shape of the M_s - m_b curve in disagreement with observation, and chose a different ensemble autocorrelation function which yielded an asymptotic slope of ω^{-2} . (Aki's particular choice of an autocorrelation does not satisfy Haskell's criterion that the earthquake begin and end in a state of static equilibrium. However, a different autocorrelation function, which would satisfy the equilibrium criteria, could be selected which would still result in an ω^{-2} asymptotic slope.)

Savage (1966) extended Haskell's 1964 non-statistical theory to handle the case of a dislocation nucleating at a point in the fault plane and spreading circularly to the boundaries of an elliptical fault. (Haskell (1964) had assumed that the fault started on a line across the width of a narrow fault and propagated down the length of the fault). Savage showed that while the simple ramp displacement function

yielded a displacement spectrum asymptotic as ω^{-2} in Haskell's initial line dislocation model; it resulted in an ω^{-3} asymptote when the more realistic initial point dislocation was assumed. This, he showed, was due to the fact that the radiating surface grew quadratically with time instead of linearly. This ω^{-3} asymptote was corroborated by Molnar, et. al, (1973) for cases in which the fault rupture velocity is less than the shear velocity.

Brune (1970) presented a shear wave source theory which brought together in a physically reasonable way several important concepts. He made plausible the idea that until influences from the ends of the fault were felt, the fault displacement after cracking would be a ramp function proportional to $\frac{\sigma t}{\mu}$, where σ is the stress and μ is the shear modulus. Assuming then, in effect, that the entire fault began to radiate at once, the characteristic period for the radiated shear energy became L/β , where L is the fault length and β is the shear velocity. Brune's shear wave displacement spectrum decayed asymptotically as ω^{-2} . This slope was not strictly speaking derived, but simply followed from his assumed form for the far-field solution which he chose to be in agreement with the result for an instantaneous stress pulse applied to the interior of a spherical surface (see Bullen, 1963). This, of course, is not necessarily a good model of a growing displacement nucleating at a point on the surface of a plane or spherical surface. (The fact

that Bullen [1963] and Randall [1966] found corner frequencies proportional to L/β for shear and L/α for compressional motion reflects the fact that their source was assumed to act instantaneously, and not the fact that the source was distributed over a volume instead of a surface, as suggested by Molnar et al. [1973]).

In his 1970 paper Brune introduced the concept of partial stress drop, ϵ , and showed that it could lead to a spectral slope of -1 somewhere between zero frequency where the displacement spectrum is flat, and asymptotic frequencies where an exponent of -2 obtains. Savage (1972) and others have pointed out that for a long thin fault one must expect $\epsilon \leq W/L$ where W is the fault width due to binding of the fault at the sides.

Contemporaneous with his theoretical paper, Brune and a number of co-workers analyzed signals from many earthquakes and tried to interpret them in its light: see, for example, Trifunac and Brune (1970), Wyss (1970), Wyss and Brune (1971), Wyss and Hanks (1972), Hanks and Wyss (1972), Molnar and Wyss (1972), Wyss and Molnar (1972). One of the most interesting findings of these analyses is that the P wave corner frequency is higher than the S wave corner frequency. Hanks and Wyss (1972) attempted to explain this fact by replacing β in Brune's (1970) theory by α , the compressional wave velocity, and appealing to the concept of characteristic wavelength. They pointed out, however, that there was no theoretical foundation for these procedures. Indeed

Savage (1972) pointed out that the more precise theories of Haskell (1964) and Savage (1966) predict approximately equal corner frequencies for P and S waves, due to the fact that the corner frequencies are dominated by the duration of faulting, so long as that time is greater than L/β , and not by the length of the fault per se.

Molnar, Tucker, and Brune (1973) have reported that the P wave corner frequency is higher than that of the S wave corner for 144 aftershocks of the San Fernando February 9, 1971, earthquake. They also show by an exact solution, following Savage (1966), that the P-corner is higher than the S-corner if the strain is released instantaneously over the entire surface of a circular disk. On the other hand, if the dislocation propagates at about 0.5 times the S wave velocity then they find that the two corner frequencies are about equal. This result is in agreement with the studies of Haskell (1964) and Savage (1966, 1972).

At intermediate dislocation velocities the results of Savage (1974) show the importance of the operational definition of corner frequency. Savage (1974) shows that if the corner frequency is defined as the intersection of the high frequency displacement asymptote with the horizontal low-frequency asymptote, then if v , the dislocation velocity, is close to the shear wave velocity the P wave corner will be substantially higher than the S wave corner. On the other hand, examination

of Savage's Figures 1 and 2 shows that for the same cases the P wave corner will be on the order of only 20% higher than the S wave corner if the corners are taken as the 6dB (1/2 amplitude) points on the displacement amplitude spectrum. The identical conclusions can be obtained by examination of Figure 6 in Molnar et. al. (1973). In fact, one sees there the special dangers of the asymptotic definition of corner frequencies in that for $v=\alpha$, where α is the compressional wave velocity, the intersection definition gives $f_p < f_s$ for $\theta=85^\circ$, an observation point near the plane of the fault. This result is easily verified from Savage's (1974) figures, and one may see also that for the 6dB corners, $f_p > f_s$. These results suggest that the 6dB corner determination is more reliable than determination by the intersection of asymptotes. It is probably just as "objective" as the intersection of asymptotes method, and is certainly not as severely affected by incorrect values of Q, a serious problem with the latter method as pointed out by Thatcher and Hanks (1973).

We show in this paper that another explanation of the $f_p > f_s$ paradox may be found by further development of Haskell's (1964, 1966, 1972) ideas that a substantial amount of tensional faulting accompanies many strike-slip or dip-slip earthquakes, and that many earthquakes are accompanied by smaller earthquakes. There is substantial evidence for this point of view in the literature. Wyss and Brune (1967) concluded

that the 28 March 1964 Alaskan earthquake ruptured in a series of events; initially propagating in various azimuthal directions from the epicenter, then after a period of about 44 seconds propagating steadily to the West. They also concluded that other large earthquakes are similar in character. Trifunac and Brune (1970) found that the Imperial Valley earthquake could be regarded as a series of earthquakes initiated along a strike-slip fault in accordance with $v/\beta \approx .5-.6$. Kamb et. al. (1971) show that the pattern of near-surface faulting for the San Fernando earthquake was very complicated, and Jungels and Frazier (1973) conclude that this complexity must be taken into account in order to satisfactorily interpret the static displacement observations. One might speculate that if the near-surface faulting is complicated, so too must be the deeper faulting. Jungels and Frazier also require changes in dip for the fault plane. Bolt (1972) analyzed the Pacoima Dam strong motion records for the San Fernando earthquake and concluded that several "bursts" of high frequency energy were received from remote epicenters on the fault plane. Mikumo (1973) discusses the substantial field evidence for flexures in the San Fernando fault plane before adopting a plane surface for his theoretical model. Murray (1973) has concluded that the main Parkfield earthquake consisted of two separate earthquakes on two branches of the San Andreas.

It seems, in fact, that almost every carefully investigated earthquake reveals first-order departures from a plane slip fault. This, of course, is not surprising given the inhomogeneities of the real earth. Tensional sub-earthquakes must also be expected. Although a homogeneous substance may fail in shear, one must expect zones of weakness in an inhomogeneous material to "pull apart", thus introducing a tensional component to an earthquake. Alternatively, if a fault plane is curved and strike-slip movement occurs, one expects some separation on the curves.

The above remarks are not meant to deny that the best initial approximation to almost all earthquakes is slip on a plane. This is strongly implied by the numerous successful studies of long-period radiation from earthquakes based on the double-couple model. However, one might reasonably expect the high-frequency displacement spectrum asymptotes to be severely affected by small tensional sub-earthquakes.

Another puzzling contradiction between theory and observation has been the apparent S/P amplitude ratio, as observed on velocity or acceleration seismograms, of about 3/1, whereas theory, e.g. Haskell (1964), predicts a ratio closer to 10 or 20 to 1. The possibility that observations are affected by unknown variations in Q between S and P waves somewhat confuses the issue. The most reliable data is presumably that from closest in, and Trifunac and Brune (1970) show

strong-motion seismograms where the ratio for the 1940 Imperial Valley subearthquakes vary between 10/1 and 1/1 with a mean around 3/1. The first six minutes of aftershocks of the February 9, 1971 San Fernando Earthquake as recorded at the Pacoima Dam strong motion instrument also give a mean ratio of about 3/1, as we shall see in later sections of this report. As pointed out by Haskell (1964), this paradox could be resolved if much of the energy around the corner frequency came from tensional faulting for which the theoretical amplitude ratio is about 3/1.

Among the important observations which a successful source theory should address are those which have grown out of the efforts to discriminate earthquakes from underground explosions. The amplitude of twenty-second Rayleigh waves plotted versus the amplitude of one-second compressional waves is known to be an excellent discriminant; see for example Evernden et. al. (1969, 1971) and Marshall and Basham (1972). One of Aki's (1967) chief motivations in changing from Haskell's (1966) ω^{-3} model to an ω^{-2} model was that the latter is in much better agreement with existing $M_s - m_b$ data. On the other hand, the "spread" in observed $M_s - m_b$ plots is much greater than can be accounted for by sampling, measurement, and propagation errors; and therefore any single line in $M_s - m_b$ space, such as the ω^{-2} model cannot adequately explain the data. Examples of especially discordant earthquakes that look like explosions with respect to this discriminant may be

found in Landers (1972) and Der (1973). Douglas et al. (1973a) have shown that a substantial amount of this discrepancy may be explained by assuming that the earthquakes are dip-slip with a dip of 45° . This fault-plane orientation has a radiation pattern maximum for the teleseismic P radiation. Douglas et al. and Gilbert (1973) have also shown that even for point sources the average shallow shearing earthquake will separate from shallow explosions by approximately 0.5-1.0 magnitude units. A possible physical explanation is that if one first matches the P wave amplitudes, then for the earthquake there is ten times the compressional wave amplitude emitted as shear waves. If shear waves are about as efficiently converted to Rayleigh waves at the free surface as are the compressional waves and if the earthquake is "shallow" with respect to the Rayleigh wavelength, then one expects about ten times the Rayleigh wave from an earthquake as from an explosion of equal m_b . The same argument then suggests that for tensional earthquakes one would have only about three times the Rayleigh wave amplitude.

Anglin (1971) plotted complexity versus third moment of the observed spectrum for earthquakes and explosions and found good separation. In general there is no physical explanation for the separation, and until one is presented, the weaknesses and limitations of the discriminant cannot be convincingly discussed. In this report we are able to give a plausible explanation of Anglin's results by assuming that the

more complex the earthquake, the more small earthquakes there are accompanying it. (A complicating point in this discussion is the idea developed by Douglas et al. (1973b) that complexity may be due to arrivals along separate low and high-Q paths.)

In this report we find that the high-frequency asymptotes of earthquakes can vary between ω^{-3} for simple earthquakes to $\omega^{-1.5}$, where the exponent is restrained only by the requirement for finite radiated energy (von Seggern and Blandford [1972] present evidence that the asymptote for explosions is ω^{-2}). We find that in the case of complicated earthquakes: mixing shear and tensional sub-earthquakes, any monotonically decreasing displacement spectral shape can be attained. Savage (1972) has made much the same point, saying "the spectrum of the incoherent radiation could mask the ω^{-3} asymptotic behavior". This implies that short-period discriminants may be very unreliable in practice. However, with knowledge of the underlying mechanisms it may be possible to suitably constrain the combinations of discriminants, regionalize the earthquakes, and make short period discriminants predictable and reliable.

In the following sections, we develop and apply the theory, make some comparisons with previous theoretical results, and compare some results with observation.

THEORY

Haskell (1964) gives the following expressions for the teleseismic radiation from a slip fault in a homogeneous full space:

$$\begin{aligned}\epsilon_{\alpha}(\omega) &= (\rho w^2 L^2 D_0^2 / 2\pi\beta) (\beta/\alpha)^5 |\hat{G}(\omega)|^2 B_1(\omega) \\ \epsilon_{\beta}(\omega) &= (\rho w^2 L^2 D_0^2 / 2\pi\beta) |\hat{G}(\omega)|^2 B_2(\omega)\end{aligned}\quad (1)$$

where ϵ_{α} is the total radiated compressional energy density at frequency ω , α is the compressional velocity, ω is the circular frequency, ρ is the material density, w is the fault width, L the fault length, D_0 the (constant) displacement, and β the shear velocity. $E_{\alpha, \beta}$ satisfy the relation

$$E_{\alpha, \beta} = \frac{1}{2\pi} \int_0^{\infty} \epsilon_{\alpha, \beta}(\omega) d\omega$$

where E is the total radiated energy. (Note: To change the energy spectrum to displacement amplitude spectrum, multiply by ω^{-2} and take the square root.) $\hat{G}(\omega)$ is the Fourier transform of $\ddot{G}(t)$ where $G(t)$ is the displacement time history at a point on the fault and is normalized such that $G=0$ for $t<0$ and $G \rightarrow 1$ as $t \rightarrow \infty$. $B_1(\omega)$, illustrated in Figure 1 of the theoretical results section, is asymptotic to 0.27 at low frequencies and decays like ω^{-2} at high frequencies. $B_2(\omega)$ is

similar but has a low frequency asymptote of 0.40.
 ϵ_β is the radiated shear energy.

These are Haskell's relations for a long thin fault in which rupture initiates on a line across the fault and for which the direction of slip is down the fault, parallel to the direction of rupture propagation. The effects of the velocity of rupture propagation, v , are hidden in the B functions which are defined by, for example,

$$B_1(\omega) = \int_0^\pi \sin^3 \theta \cos^2 \theta X_\alpha^{-2} \sin^2 X_\alpha d\theta \quad (2)$$

where

$$X_\alpha = \omega L(a - \cos \theta) / 2\alpha \quad (3)$$

and $a = \alpha/v$. $B_2(\omega)$ similarly involves $b = \beta/v$.

Haskell's expressions for a fault in which the displacement is in the fault plane perpendicular to the direction of rupture propagation are identical except that B_3 and B_4 replace B_1 and B_2 respectively. We shall see from graphs in the theoretical results section that the corresponding functions are almost identical.

For tensional faults (in which the displacement is perpendicular to the fault plane), the expressions are also identical except that B_5 and B_6 replace B_1 and B_2 ; and, most important, the expression for E_α has been multiplied by $(\alpha/\beta)^4$. Since the ratio B_5/B_6

is almost equal to the ratio B_1/B_2 , this means that the displacement S/P ratio for tensional earthquakes is one-third that from slip earthquakes.

Savage (1966, 1974) has shown that the corner frequencies of the radiation from a fully two-dimensional fault are determined by the time intervals between first motion and two stopping phases. Each corner frequency contributes a factor ω^{-1} to the far-field displacement amplitude spectrum. In turn, we may see by an argument much like Savage's (1966) that these times are controlled by the two principal dimensions of the fault. Consider first the case where the displacement discontinuity (let us assume a step function) nucleates at a point and propagates slowly in comparison with the wave velocity. The radiating source line grows linearly in time until it encounters the side of the fault. This occasions the first stopping phase, since the radiating line is thereafter constant in length until it reaches the end of the fault where its length goes to zero as the wavefront intersects the fault edge. This generates the final stopping phase. Clearly the corner frequencies will be proportional to v/W and v/L for both P and S waves.

In the case where $v \gg \alpha$ and β a similar argument may be made. Consider those receivers not near the perpendicular to the fault plane (as Molnar et al. [1973] and others have point out, these receivers fill the dominant portion of the focal sphere). For such

receivers the first arrival will be from that point on the edge of the fault nearest the receiver. The line on the fault from which radiation will be received will grow linearly in length as a function of time until its ends encounter the sides of the fault at a time characteristically about W/α for the P wave and W/β for the S wave. At this point a stopping phase is created as the generating line ceases to grow. The line thereafter is of constant length until it encounters the end of the fault at times about L/α and L/β for P and S respectively. Thus, as assumed by Hanks and Wyss (1972) and others and as shown explicitly by Molnar et al. (1973) and Savage (1974), one can obtain different P and S corner frequencies if $v \rightarrow \infty$. Whether this is a realistic model is another matter. Note that this analysis does not explicitly call on diffraction theory to justify the location of the corner frequencies. With further geometrical insight one can see that these times should be multiplied by $\sin\theta$, where θ is the angle between the perpendicular to the fault and the direction of wave propagation. Other qualitative aspects of the radiation can be deduced according as the direction of wave propagation is almost parallel to the short or long sides of the fault. A rather complete picture of the radiation can be built up from physical arguments without mathematics. See Savage (1966) for a detailed discussion.

We can now see that Haskell's (1964) analysis of a long thin fault assumes in effect that v/W is a

substantially higher frequency than those under observation. We can also see that contributing to the ω^{-2} asymptotic spectrum obtained by Haskell is ω^{-1} from the B function appropriate to L, and ω^{-1} from his assumed ramp time function. It is clear, as pointed out by Savage (1972) and confirmed by Molnar et al. (1973), that a ramp time function in connection with a realistic fault must generate an asymptotic spectrum proportional to ω^{-3} . A minor exception occurs in the case of a circular fault where the displacement nucleates at the center. The simultaneous stopping along the whole length of the line source generates a sharp discontinuity in the radiated trace resulting in $\omega^{-2.5}$ Savage (1974, 1966). Something so perfectly symmetrical would be unlikely to occur in the earth.

Archambeau's (1968) relaxation theory also results in a spectrum asymptotic as ω^{-3} (Archambeau, personal communication; Minster (1973)). However, the relation of this result to our displacement models is unclear.

In this report we modify Haskell's solutions to take account of a finite value for W, by multiplying equations (1) by an additional factor B_1 and B_2 as appropriate; except that L in (3) is replaced by W.

$$\begin{aligned}\epsilon_{\alpha}(\omega) &= (\rho W^2 L^2 D_0^2 / 2\pi\beta) (\beta/\alpha)^5 |\hat{\ddot{G}}(\omega)|^2 B_1^L(\omega) \cdot B_1^W(\omega) \\ \epsilon_{\beta}(\omega) &= (\rho W^2 L^2 D_0^2 / 2\pi\beta) |\hat{\ddot{G}}(\omega)|^2 B_2^L(\omega) \cdot B_2^W(\omega)\end{aligned}\tag{1'}$$

This results in a solution which has the proper qualitative properties such as generation of high-frequency shear waves when $v \approx \beta$, generating waves which approximate a shock, corner frequencies as appropriate to W and L , and ω^{-3} displacement asymptotes. In view of these correct qualitative features we are certain that the conclusions reached in this report are accurate. It must be admitted, however, that a more satisfactory solution would be to use solutions such as those presented by Molnar et al. (1973) and Savage (1974) averaged over the focal sphere for a suitable non-circular fault surface. This would be, however, a difficult calculation. We have therefore fallen back to an approximate generalization of Haskell's (1964) solution which he, of course, had already integrated over the focal sphere. We might remark that one restriction in Haskell's analysis results from the fact that he represented the B integrals as the sum of two separate integrals, each of which diverges if $v > \beta$ but whose sum is finite, as are the basic integrals (2). Thus in this report we are able to give no results for $v > \beta$.

Returning to equation (1') we need an expression for the function G . In this we follow Brune (1970) and write:

$$G(t) = D(t)/D_0 \quad (5)$$

$$D = 0, \quad t < 0 \quad (6a)$$

$$D = \frac{\sigma\beta}{\mu} \tau \left(1 - e^{-t/\tau} \right), \quad 0 < t < \epsilon' \quad (6b)$$

$$D = \frac{\sigma\beta}{\mu} \tau \left\{ \left(1 - e^{-t/\tau}\right) - (1-\epsilon) \left(1 - e^{-(t-\epsilon')/\tau}\right) \right\}, \quad t > \epsilon' \quad (6c)$$

$$\tau = \frac{L}{\beta}, \quad \epsilon' = \frac{\epsilon L}{2\beta}, \quad D_0 = \frac{\epsilon\sigma\beta\tau}{\mu} = \frac{\epsilon\sigma L}{\mu} \quad (7)$$

$$|\ddot{G}(\omega)|^2 = \frac{\omega^2}{\epsilon^2 \tau^2} \frac{1}{\omega^2 + \tau^{-2}} \left\{ (2-2\epsilon) (1 - \cos(\epsilon'\omega)) + \epsilon^2 \right\}. \quad (8)$$

Here we see expressed Brune's idea that a stress pulse σ is applied to the surface of the fault in a medium with shear modulus μ , and the displacement grows linearly with time as a ramp function until approximately the time τ , when elastic waves return from the edges of the fault and bring the motion to a gradual halt. These ideas have received experimental confirmation in work by Johnson, Wu, and Scholz (1973) and by Brune (1973). If there is partial stress drop, then at a time ϵ' a reverse stress is applied whose resulting motion also comes to a completion in time τ and reduces the final displacement from $(\sigma/\mu)L$ to $\epsilon(\sigma/\mu)L$. Savage (1972) and others have pointed out that in a long narrow fault one would expect $\epsilon \approx W/L$, since the absence of slip at the edges would prevent a complete dislocation. In such a case one might better choose $\tau = W/\beta$ and do away with the second term of equation (6c) unless $\epsilon < W/\beta$. The expression for ϵ' is derived by assuming that the reverse stress is applied when the displacement has reached 1/2 its final value.

Our expression for τ is in agreement with that of Brune (1970), but the expression for ϵ' is different by a factor of slightly less than 2 if one interprets the radius of Brune's circular fault as equal to $L/2$. Such a disagreement is easily understandable in view of our slightly different formulation of the problem, and an exact answer is undoubtedly meaningless since in both cases the motion on the fault is prescribed and is not a solution of the dynamical equations. It seems doubtful that it is possible to guess the dynamical motion on the fault to better than a factor of 2. We shall see in later sections that an error in ϵ' of a factor of 2 would have no significant effect on the important results of this report.

Equation (8) is the modulus squared of the Fourier transform of $G(t)$. The expression within curly braces is the square of Brune's $F(\epsilon)$. We see that the asymptotic behavior of $|\ddot{G}|^2$ is ω^0 . Together with the ω^{-2} of B this yields ω^{-4} for ϵ_α (with two B functions) and ω^{-3} for the displacement.

To introduce the ideas of "subearthquakes" developed in the Introduction, we simply sum together the energy from all the earthquakes which are considered to make a contribution. Here we are assuming that the subearthquake radiation is incoherent with respect to all other earthquakes. (For identical fault orientations and slips this would not be true for the lowest frequencies. We assume that the total effect of such

subearthquakes is negligible at low frequencies.) The displacement is then calculated by multiplying the sum spectrum by ω^{-2} and taking the square root.

Because of success by many workers in analyzing the long-period radiation from earthquakes in terms of the simple double-couple model, we allow the moment of the earthquake to be perturbed by subearthquakes by substantially less than a factor of 2. As we shall see, this places practically no restrictions on the shape and character of the higher frequency event spectra. We assume that the subearthquakes are composed in equal parts of slip in the direction of their own fault propagation, slip in the plane perpendicular to the direction of fault propagation, and tensional motion perpendicular to the fault plane. Each of the three subearthquake types is assumed to contribute equally to the submoment.

In principle each subearthquake can have subearthquakes of its own. We investigate this infinite regression to depths up to $n=6$. For lack of a better assumption, or suitable data, we assume that each sublevel entering makes an equal contribution to the total submoment. This assumption will be seen to require increasingly many earthquakes at each sublevel.

There is of course a distribution of the size of subearthquakes ranging from the size of the main earthquake down to millimeters. A sample of such a distribution is, however, unknown from observation or theory and so we assume in this report that it is given by a

delta function at some fractional length (r^n for the n 'th level) smaller than the main earthquake. We assume also the same shape and the same values for σ , μ , β , α , v and ϵ . Each of these assumptions could, of course, be relaxed if data or a reasonable hypothesis suggested otherwise. We choose them only because they are about the simplest possible assumptions. Physically, they amount to Aki's (1967) similarity hypothesis, although we make the hypothesis here for subearthquakes rather than a set of separate earthquakes. Also, each individual earthquakes's asymptotic spectrum decays as ω^{-3} instead of ω^{-2} as in Aki's theory.

Given the assumptions discussed in the two paragraphs above, if the additional submoment is M_a , and if there are a total of N sublevels, then the number of earthquakes of a given type (two slips, one tensional) on sublevel n is given by:

$$N_a = \left\{ M_a \left(\frac{1}{3N} \right) \left(\epsilon \sigma L^2 W / \mu \right)^{-1} r^{-3n} \right\}^2. \quad (9)$$

We have explicitly assumed in deriving this equation that the low-frequency "moment" radiation from the subearthquakes is incoherent. Differing fault plane orientations could easily cause this even if the faults were all slip or all tensional.

For explosions we base our analysis on the HARDHAT granite data of Werth and Herbst (1963) as analyzed by von Seggern and Blandford (1972). von Seggern and Blandford followed the general analysis techniques of

Haskell (1967), but where Haskell only allowed the reduced displacement potential to imply a step in the derivative of acceleration, von Seggern and Blandford allowed a step in velocity. This assumption seemed to be in better agreement with the near-field data and resulted in an asymptotic displacement spectrum proportional to ω^{-2} instead of ω^{-4} as found by Haskell (1967). This scaling also allowed von Seggern and Blandford to fit teleseismic data from Longshot, Milrow, and Cannikin more accurately.

An apparent deficiency of Haskell's (1967) ω^{-4} explosion model which prompted von Seggern and Blandford's work was the fact that at high frequencies explosions gave a decreasing amplitude spectrum as a function of yield. Thus for large enough yield, cube root scaling would give decreasing m_b values. A similar phenomenon occurs in the ω^{-3} earthquake spectra in this report. One obtains a constant m_b as fault length increases. At a low magnitude the M_s - m_b curve turns up sharply, in disagreement with observation. Haskell's (1966) ω^{-3} statistical earthquake model implied the same disagreement and this prompted Aki (1967) to propose his ω^{-2} model. In this report we satisfy observation by allowing subearthquakes.

The expression for the explosion far-field energy spectrum from von Seggern and Blandford (1972) is:

$$\epsilon_{\alpha}^x(\omega) = (8\pi\rho\psi^2(\infty)\omega^2/\alpha) \frac{[(1+2B)(\omega/k)^2+1]}{[(\omega/k)^2+1]^3}$$

$$\Psi(\infty) = \psi_0 \left(\frac{Y}{Y_0} \right), \quad k = k_0 \left(\frac{Y}{Y_0} \right)^{-1/3} \quad (10)$$

Here $\Psi(\infty)$ is the long-time asymptotic reduced displacement potential, B is a dimensionless constant, and k is a characteristic frequency. Cube-root scaling implies the other relations in (10), where ψ_0 and k_0 are observed values from a scaling event. Using Werth and Herbst's (1963) data for HARDHAT, von Seggern and Blandford find $B = 2.04$, $\psi_0 = 2.5 \times 10^9 \text{ cm}^3$, $Y_0 = 5$ kilotons, $k_0 = 16.8 \text{ sec}^{-1}$.

From Haskell (1967) we have for the explosion displacement spectrum at radius R ,

$$U_{\alpha}^x = (2\rho\alpha 4\pi R^2\omega^2)^{-1/2} [\epsilon_{\alpha}^x(\omega)]^{1/2}. \quad (11)$$

The corresponding expressions for earthquakes are:

$$\begin{aligned} U_{\alpha}^e &= (2\rho\alpha 4\pi R^2\omega^2)^{-1/2} [\epsilon_{\alpha}(\omega)]^{1/2} \\ U_{\beta}^e &= (2\rho\beta 4\pi R^2\omega^2)^{-1/2} [\epsilon_{\beta}(\omega)]^{1/2}. \end{aligned} \quad (12)$$

THEORETICAL RESULTS

In Figure 1 we see B_1 and B_2 presented as a function of $p = \omega L/\alpha$ or $\omega L/\beta$ as appropriate. We choose $v = 0.775\beta$ and $\alpha = \sqrt{3}\beta$ so that these are identical to the functions graphically displayed by Haskell (1964).

In Figure 2 we compare the B functions for the three types of fault discussed by Haskell (1964). We see that they are quite similar and could probably be replaced by one function for P and another function for S for most qualitative and quantitative purposes.

It might be suggested that in equations (1') we should use B_1B_3 and B_2B_4 instead of B_1^2 and B_2^2 , since for a fault nucleating at a point, half the fault slips in the direction of propagation, and half at right angles. However, inspection of Figure 2, in connection with other results to be discussed, will show that the net effect would be negligible.

Figure 3 illustrates the effect of increasing or decreasing the velocity of rupture. As mentioned in the Theory section, Haskell's analytical approach makes it impossible to calculate solutions for $v \geq \beta$. One easily sees that lower velocities reduce the radiated energy and decrease the S/P ratio. Another interesting feature is the introduction of an apparent ω^{-1} intermediate trend for $v \approx \beta$. This probably means that the low-frequency shear waves have formed a shock wave, but the higher frequency waves are still not in phase. Similar behavior in the near-field was noted by Aki (1968). Thus we have another cause for an intermediate

trend in the displacement spectrum, in addition to fault width and partial stress drop. Among authors who have discussed the possible velocities of fault rupture are Mansinha (1964), Aki (1968), Weertman (1969), Wyss and Brune (1967), Murray (1973), and Boore, Aki, and Todd (1971).

Figures 4 and 5 illustrate the same conclusions for the other two types of fault except that the intermediate frequency trend is not so apparent.

Next we carry the analysis to the displacement spectrum given by (11). Throughout this report the earthquake parameters given in Table 1 are held fixed. The parameters L , v , ϵ , n (the number of levels of sub-earthquakes), r (the ratio of lengths of successive subearthquakes), and earthquake type vary, and are indicated as appropriate on each Figure. We choose the letters SS, DS and T to indicate the main earthquake type; respectively, slip in direction of propagation, perpendicular to direction of propagation but in fault plane, and perpendicular to the fault plane. Solutions for other values of σ may be obtained by scaling the displacements up or down in proportion to ($\sigma/100$ bars).

Table 1

Earthquake Parameters Fixed in this Report

$$\begin{array}{lll} \sigma=100 \text{ bars}=10^8 \text{ dyne cm}^{-2} & \alpha=8.0 \text{ km/sec} & \rho=3.0 \text{ gr cm}^{-3} \\ \mu=3.0 \times 10^{11} \text{ dyne cm}^{-2} & \beta=4.62 \text{ km/sec} & R=8.0 \times 10^3 \text{ km} \\ W=L & & \end{array}$$

In Figure 6 we have plotted the displacement spectra

for P and S, and their ratio. Note that the corner frequencies for S and P (indicated by filled circles on this and subsequent Figures) are almost equal. Note also that the P/S ratio is about 0.13 decreasing to about 0.05 for higher frequencies. The sharp dip around 1.7 Hz is probably not realistic, for two reasons: first, as we noted above, use of $B_1 B_3$ instead of B_1^2 is probably more realistic and would smooth out this null; second, in the real earth any null this sharp is usually smoothed out by effects not considered here.

Next we investigate the effect of subearthquakes by adding to the simple type SS fault just discussed equal numbers of fault types SS, DS, and T with lengths = $L/3 = 1.05$ km., in sufficient quantity to increase the long period P displacement radiation by about 25%; and the long-period S radiation by about 10%. We see in Figure 7 that as a result ω_p is higher than ω_s by a factor of 1.7, and the high-frequency P/S ratio varies between 0.17 for low frequencies to 0.28 for high frequencies. Note also that it would be extremely difficult to determine ω_s by use of the high-frequency asymptote since the spectrum has a rather uniform curvature at high frequencies. We see also in Figure 7 the definite suggestion of an intermediate slope. This last effect of the subearthquakes would be created no matter what their type. But the shift in relative corner frequency and the increase in P/S ratio at high frequencies are due solely to the presence of 1/3 tensional subearthquakes. Since their P energy is comparatively high, and since earthquakes of any size of a given type have equal high-frequency

displacements (because of the ω^{-3} asymptotes), almost all the high-frequency P wave energy comes from the several small tensional subearthquakes. Therefore ω_p is larger than ω_s whose value is not so severely affected by the subearthquake energy.

Figure 8 shows explicitly how simple earthquakes of different sizes have identical high-frequency displacement spectra. The "periodicity" in the P/S ratio illustrates the fact that exactly the same B functions are shifted left and right along the frequency scale to produce plots for different size earthquakes.

Figure 9 shows explicitly the P/S ratio for different types of earthquakes. We see that at all frequencies the tensional earthquakes have about 3 times the compressional amplitude of slip earthquakes.

Figure 10 adds to the energy spectra of Figure 9 the energy spectra from equal numbers of fault types SS, DS, and T with lengths $L/3 = 1.05$ km in sufficient quantity to increase the long-period P displacement by about 25%, and the long-period S radiation by about 10%. We see that the spectra including the SS and DS principal earthquakes become identical to each other, the same as we have seen already in Figure 7. The spectrum including the principal T earthquake is equal to the other two above 1.0 Hz, but below 1.0 Hz has about 3 times the P wave amplitude.

In Figure 11 we investigate the effects of different values for n . Recall from the Theory section that we force each sub-level to make an equal contribution to the total moment, but do not allow the total

moment to change as n increases; see equation (9). As might be expected we are able to move the P wave corner frequency arbitrarily high. It seems clear also that earthquakes of greatly differing size from a single region might have the same corner frequency if the smallest subearthquakes were always the same size, perhaps being controlled by the lack of rock joints below a certain scale.

In Figure 12 we vary the total moment of the subearthquakes and see that once the total moment rises above, say 10% of the original, the effect on corner frequency is established, and further increases do not seem to change the situation substantially. It is noticable, however, that subearthquakes that create undetectable amplitude changes at frequencies as high as 0.4 Hz can have an important influence on P/S ratios around 2.0 Hz.

In Figure 13 we vary the value of r while maintaining the total moment constant and using only $n=1$. As might be expected, we see that the smaller earthquakes have the more profound effect on corner frequencies and P/S ratios (of course, were their number not increased according to (9) in order to maintain constant moment, the smaller subearthquakes would have a smaller effect).

Figure 14 shows the effect on simple earthquakes of variation in v , the rupture propagation velocity. As we saw in connection with Figure 4, an intermediate

ω^{-1} spectral trend with frequency emerges at the higher velocities. Note also that the large velocities create very low P/S ratios at high frequencies-on the order of 0.01. This occurs because of the great enhancement of the S wave spectra in shock formation.

In Figure 16 we introduce variation in ϵ for a simple earthquake and see that shift in moment and the appearance of an intermediate spectral trend with frequency as shown by Brune (1970). As can easily be seen from the structure of equation (1'), changes in ϵ do not affect the P/S ratio, and this can be seen explicitly in Figure 16. From this fact one would expect that while the P and S corner frequencies might shift with ϵ , they would not shift relative to one another. We see from Figure 16 that this is in fact true, and also that the corner frequencies themselves change by less than 20%.

Figure 17 illustrates the results when one level of subearthquakes with the appropriate values of ϵ are added to the simple earthquakes of Figure 16.

We might repeat at this point that solutions for other values of σ or μ can be obtained by shifting lines in Figures 6-17 up or down the page, since these parameters appear only as multiplicative constants; see equations (1', 5, 7, 8). This also shows explicitly that earthquakes of greatly different magnitudes may have the same corner frequency.

Next we discuss the theoretical results in terms of their impact on the M_s - m_b discriminant. Rather than try at this point in the report to relate the displacement values calculated at .05 and 1.0 Hz to M_s and m_b values, we shall first make whatever deductions are possible by simply assuming proportionality between log displacement and magnitude. We shall, however, slightly anticipate later arguments by plotting the root-mean-square compressional plus shear displacement for the 0.05 Hz displacement. All conclusions reached in this report would, however, have been identical had we used only the shear displacement, since the root-mean-square is only the order of 5% greater. For the 1.0 Hz displacement we use, of course, only the compressional wave displacement.

In Figure 18, we see the M_s - m_b relation for simple earthquakes. For the smaller fault lengths where the corner frequency is above 1.0 Hz, the spectrum is flat between 0.05 and 1.0 Hz and therefore M_s is proportional to m_b . Between $L = 1.0$ and 3.16 km the corner frequency passes through 1.0 Hz and the displacement at 1.0 Hz becomes nearly constant. With increasing L the 0.05 Hz displacement continues to increase. This, of course, results in a nearly vertical M_s - m_b line. Around $L = 31.6$ kilometers the corner frequency becomes lower than 0.05 Hz, and M_s no longer increases significantly.

The resulting M_s - m_b line is strikingly different from those observed, e.g. Evernden et al. (1969, 1971).

As mentioned before, such a line is a necessary result of any ω^{-3} model. This disagreement with observation drove Aki (1967) to consider ω^{-2} models. Let us note at this point, however, that we have assumed $\sigma = 100$ bars for all calculations in this report. Thatcher (1972), Thatcher and Hanks (1973), and others have documented σ values ranging roughly from 0.2 to 200 bars. Hanks (1974) has deduced by analysis of the Pacoima Dam seismograms stress on the order of 350-1400 bars near the epicenter of the San Fernando earthquake. Accordingly, any point on Figure 18 could be moved diagonally as much as 3-4 magnitude units. It can be seen that this corresponds to the fact that variation in σ produces a straight line in the Ω_0 - f_0 (moment-corner-frequency) diagrams of Hanks and Thatcher (1972) and Thatcher and Hanks (1973). Thus, even a region with only simple earthquakes could have a wide range of possible M_s - m_b plots if there were a wide range in possible values for σ . Note, however, that none of the earthquakes would cross the limiting line which is drawn so that if the shear and compressional spectra are flat, the earthquake will lie upon it.

In Figures 19-22 we show the effects on the M_s - m_b plot of 2, 4, or 6 levels of subearthquakes. We consider subearthquakes for which $r = 0.33$ or 0.57 , and in which the additional moment is constrained to be equal to those indicated by lines 3 or 5 in Figure 12. These two levels represent percent changes in the P wave long-period radiation of 25% and 1% respectively.

We see that above the limiting line almost any $M_s - m_b$ curve desired may be achieved, especially when one considers possible variations in σ . This can occur even though the amplitude of the P wave long-period displacement changes by less than 1%. Still, we see that there are no major excursions over the limiting $M_s - m_b$ line. The few small violations that do occur may be traced to the influence of tensional subearthquakes.

In Figures 23-25 we see that with $n=4$ a variation of ϵ and/or v can give a rather reasonable $M_s - m_b$ curve, and with variations in σ might be adjusted even closer to observation. Obviously we have embarrassingly many variable parameters at our disposal. However, in none of these cases is there a significant excursion over the limiting line.

In Figure 26 we arrive at just such a significant excursion by assuming that the basic simple earthquake is tensional in character. It is in fact easy to see that the limiting line for tensional earthquakes is about 0.5 magnitude units to the right of (or 0.35 units perpendicular to) the limiting line for slip earthquakes. There have, however, been no tensional earthquake fault-plane solutions reported in the literature, so that the existence of such simple earthquakes is in doubt.

Finally, in Figures 27 and 28 we see the explosion spectra and $M_s - m_b$ curves resulting from equations (10,11).

As an insight into the next section about comparison with observation we have placed on Figure 28 the limiting M_s - m_b line for slip earthquakes. A dashed reference line has also been drawn through the family of explosion points to show that M_s is not strictly proportional to m_b even at intermediate frequencies. In fact, we notice that the slope is less than 1.0 for intermediate yields, a result of the existence of the maximum in the spectra of Figure 27. Brune's displacement function (6) results in a no such intermediate frequency maxima for earthquakes. If one were to specify a displacement time history such as Haskell's (1964) modulated ramp because of some such physical idea as overshooting of the equilibrium displacement, then one would have another mechanism for obtaining earthquake M_s - m_b points on the lower side of the limiting line. Archambeau's (1968) theory apparently predicts such an overshoot; however, it has not been found in the experimental studies of Johnson et al. (1973) and Brune (1973).

COMPARISON WITH OBSERVATION

Douglas et al. (1973a) have calculated theoretical values for explosion M_s and m_b also assuming, as we have, Werth and Herbst's (1963) granite reduced displacement potential. They took into account the distance to the free surface, receiver and source region layering, absorption, dispersion, divergence of the P waves, instrument response, and conventional measurement techniques for M_s and m_b . For 100 kilotons in granite at a depth such that pP reinforces P they obtained $m_b = 5.2$, $M_s = 4.0$. If we subtract 0.2 m_b units as an approximation to the m_b which would be obtained for a deep shot where pP did not reinforce P, then we may appropriately calibrate Figure 28 by setting the 100 kt shot at the $m_b = 5.0$, $M_s = 4.0$ point. The result may be seen in Figure 29. This is, of course, a purely theoretical calibration, and effects such as spall, anomalous absorption, etc., may invalidate it.

To gain further insight into the nature of our solutions we superimpose Figure 29 on a figure from Douglas et al., resulting in Figure 30. The parameters for the earthquakes plotted in Figure 30 are given in Table 2 taken from Douglas et al. Some of these points were misplotted in their original figure, and the appropriate corrections have been made in Figure 30. We see that some explosion points fall to the left of our granite line. This may be traced to

TABLE 2
Earthquake Parameters for Earthquakes Plotted in
Figure 30. From Douglas et al. (1973).

Fault orientation	Dimensions of fault plane	Depth of focus (km)	Period of zero in surface wave specimen (s)	Amplitude of 20-s period (μ)	Surface wave magnitude M_s	Body wave amplitude (nm)	Body wave period (s)	Body wave magnitude m_b	$m_b - M_s$
Vertical dip slip	1-km radius	15	∞	0.6	4.0	1.5	1.1	4.0	0.0
	1-km radius	10	∞	0.8	4.1	1.5	1.1	4.0	-0.1
	8×0.5 km	15	∞	1.2	4.3	1.0	1.4	4.0	-0.3
Vertical strike slip	1-km radius	15	20	0.04	2.8	1.6	1.1	4.0	1.2
	1-km radius	10	14	0.3	3.6				
	8×0.5 km	15	20	0.06	3.0	0.3	1.4	3.5	0.5
45° dip slip	1-km radius	15	32	0.5	3.9	9.5	1.1	4.8	0.9
	1-km radius	10	24	0.2	3.6				
	8×0.5 km	15	32	0.8	4.1	1.8	1.4	4.3	0.2

cancellation of P by pP from explosions buried at the minimum containment depth. Thus in this way explosions can be made "anomalous", at the possible risk of subsidence craters, surface leakage of radioactivity, etc. Note in Figure 30 that explosions in other materials are less earthquake-like, although the corresponding reduced displacement potentials may not be as reliable.

The earthquake models assumed by Douglas et al. were typically 2 km in diameter; the assumed displacement time history was a step nucleating at a point and spreading to the perimeter of an ellipse (basically Savage's 1966 model). The step time history will cause high frequency displacement to fall off proportional to $\omega^{-1.5}$ for the circular fault as discussed by Savage (1974) instead of ω^{-3} as in our model. Thus the 2 km diameter faults of Douglas et al. correspond most closely in Figure 18 to the 1 km length fault. Notice that this is just at the break point where the $M_s - m_b$ line for simple earthquakes begins to depart dramatically from observation. We may therefore regard the earthquake calculations of Douglas et al. to be for point sources with respect to $M_s - m_b$.

Thus the fact that our limiting line lies below but close to most of the earthquakes justifies the implicit assumption we discussed in the Introduction. That is, for point sources when P wave amplitudes are matched, earthquakes will have a larger M_s because they emit an equal amount of long-period P as do

explosions, plus about ten times the P wave amplitude as shear waves. If we may assume the absence of radiation pattern effects, and that S waves convert to Rayleigh waves as well as do P waves, then we may anticipate a full magnitude separation in the $M_S - m_b$ lines.

The earthquakes which do cross the limiting line in Figure 30 illustrate the weaknesses in the assumption of no effects due to radiation pattern. The triangles correspond to earthquakes at a depth such that there is a null in the 20-second Rayleigh radiation. This misclassification would be overcome by measurement of the maximum Rayleigh motion instead of restricting the measurement narrowly to the 20-second period. The low ($M_S - m_b$) earthquake at $m_b = 4.8$, $M_S = 3.9$ corresponds to a 45° dip-slip event which has a maximum in the P radiation for teleseismic distances. Such events would also be especially difficult to discriminate because they can display compressional first motion at all teleseismic stations. Since rarefactions have been observed at distances of 5° from Der's (1973) low ($M_S - m_b$) events, the events cannot be purely tensional in character. This leaves the possibility of a complex 45° dip-slip event, or possibly some unknown path or depth effect.

In Figure 31 we have superimposed our theoretical lines on the data of Evernden et al. (1971). We see that most of the explosions lie to the left of the theoretical granite line. This is probably because

they were fired at the minimum containment, depth, resulting in interference between pP and P. The fact that the largest explosions do not follow the granite line's curvature is probably due to the fact that m_b is being measured at frequencies less than 1.0 Hz, and also because the greater confining depth has reduced the effect of the pP-P cancellation.

The limiting line for earthquakes seems to be in good agreement with the observations. This suggests that few of the earthquakes in the sample were dominated by tensional or 45° dip-slip faulting, or had displacement time histories characterized by an overshoot of the equilibrium position.

Inspection of Figure 18 shows that there is a limit of about 4.4 M_s units between the limiting line and the highest possible earthquake. In Figure 31, this difference is only about 1.0 magnitude unit, suggesting that there are not many simple earthquakes in the Southwest United States. M_s - m_b diagrams by other authors, e.g. Marshall and Basham (1972) show a spread of two magnitude units for Eurasian events. Since even earthquakes of $L=10$ (see Figure 18) imply $\Delta M_s \approx 3$, there are apparently few simple earthquakes in Eurasia.

The success of this comparison with observation suggests that the proper way to align M_s - m_b plot of events from regions where there have been no explosions is, after station corrections have been determined and applied, to draw the limiting line and align it with some standard such as the one in Figure 31.

Next we consider the questions on observations of S/P amplitude ratios and their connections with corner frequency. Probably the best data available consist of the Pacoima Dam records of the first six minutes of aftershocks of the San Fernando earthquake. Both P and S waves are accurately recorded because an 0.5° tilt caused by the major earthquake closed the instrument's trigger and caused the instrument to run continuously. In addition, the epicenters were only about 10 kilometers distant and 10 kilometers below the surface, so that effects of absorption and interaction with the free surface were at a minimum.

The acceleration seismograms are shown in Figure 32, taken from Trifunac (1972). The brackets indicate the P and S wave windows used by Trifunac in his accelerogram spectral analyses. These spectra are displayed in Figure 33. Even a cursory inspection of Figure 32 shows that the P/S ratio is much closer to 0.3 than to 0.03, as predicted by the theory of the simple earthquake. More quantitatively, measurement of the levels of the high-frequency asymptotes in Figure 33 shows that the median ratio is 0.37.

Inspection of the records also shows that the P waves are of higher frequency than the S waves, and Figure 34 (from Molnar et al., 1973, after the data in Trifunac, 1972) shows this explicitly. In the context of the present theory these results imply that these San Fernando aftershocks (of magnitude typically $m_b = 5$) are not simple events, but have some tensional

subfaulting. Figure 35 (from Molnar et al., 1973) shows the ratios of corner frequencies from later San Fernando earthquakes ranging in magnitude from 0.5 to 4.5 M_L .

Work with teleseismic data by Wyss (1970), Wyss and Hanks (1972), Wyss, Hanks, and Liebermann (1971), Hanks and Wyss (1972) Wyss and Molnar (1972), and Molnar and Wyss (1972) has reached similar conclusions, but the Q corrections are large and uncertain.

Finally, Figure 36 displays the third moment of frequency versus complexity discriminant (from Anglin, 1971). Anglin has indicated a trend for earthquakes in which increasing complexity leads to higher frequencies. Perhaps this could be understood as follows: Complex earthquakes imply many subearthquakes, which in turn implies a higher frequency signal. A correlation might then also be sought between complex earthquakes and those close to the limiting $M_s:m_b$ line. An understanding of short-period discrimination is crucial because despite several other observational studies, e.g. Booker and Mitronovas (1964), Lacoss (1969), Ringdal and Whitelaw (1973) and Manchee (1972) analysis mostly proceeds in the dark as far as theory is concerned.

SUMMARY AND SUGGESTIONS FOR FURTHER RESEARCH

We have developed a theory which accounts for the observed separation between $M_s:m_b$ lines for earthquakes and explosions, and also explains the robustness of the discriminant despite wide ranges in earthquake (M_s-m_b) values. This wide range is explained as being due to the existence of both simple and complex earthquakes. One also sees that the difference (M_s-m_b) can be a good discriminant even though the slope of the earthquake $M_s:m_b$ line is not 1.0.

The fact that P/S ratios are closer to 0.3 than to 0.03 as classically predicted, together with the observations of higher P than S corner frequency, have been shown to be related phenomena and explainable in terms of tensional subearthquakes.

A tentative explanation has been given for the success of the complexity-third moment of frequency discriminant (we might note that this discriminant is vulnerable to evasion techniques).

The results suggest that the projected intersection of the earthquake and explosion populations suggested by the data of several workers, e.g. Marshall and Basham (1972), would not occur if data at lower magnitudes were obtained. Aside from displacement overshoot, the only method for obtaining convergence of the populations would be for small events to preferentially draw relaxation energy from small source regions as in the theory of Archambeau (1968). This possibility lies outside the scope of the present theory. Mean

$M_s:m_b$ regression lines appear to be somewhat lacking in physical significance. The fact that some theoretical justification can be obtained for short-period discriminants suggests that they may be relied upon in non-evanescent situations if carefully regionalized and if care is taken to select paths unaffected by P wave multipathing.

Further research should aim at deciding if tensional subearthquakes really exist or are only a theoretical abstraction. Field, experimental, and numerical work should all have a place.

Investigation of the displacement time history near the front of the crack is important to see if on the time scale of interest teleseismically (or regionally for earthquake damage studies) the initial velocity is discontinuous as Brune (1970) suggested and as we have assumed. Brune (1973) has presented some experimental evidence to the contrary, but it is not completely clear that wave energy from regions of earlier movement has not slightly distorted the measurements. This question is, of course, crucial because the discontinuity in the displacement time history governs the far-field high-frequency asymptote, and any slope substantially different from ω^{-3} would require major changes in the theory.

The study of the distribution of subearthquakes is also crucial. We have assumed a delta function here; perhaps $N(M_0) \propto \exp(-M_0)$ could be shown to be reasonable and tested. Again, both mapping of faults in the field and experimental measurements are needed.

Although we do not expect our basic results to change, it is important to replace Haskell's original solution for the simple earthquake by an exact solution for a fully two-dimensional fault plane surface for both slip and tensional earthquakes. Here Savage's (1974) lead could be followed.

As a final point, Aki (1967) and others have pointed out that for large events m_b is not a satisfactory measure of the total 1.0 Hz energy in the signal. A suitable measure suggested by Aki is the maximum amplitude in the P coda times the "length" of the coda raised to some power between 0.5 and 1.0.

REFERENCES

- Aki, K., 1967, Scaling law of seismic spectrum, J. Geophys. Res., 72, 1217-1231.
- Aki, K., 1968, Seismic displacements near a fault, J. Geophys. Res., 73, 5359-5376.
- Anglin, F. M., 1971, Discrimination of earthquakes and explosions using short period seismic array data, Nature, 233, 51-52.
- Archambeau, C. B., 1968, General theory of elastodynamic source fields, Rev. Geophys., 6, 241-288.
- Bolt, B. A., 1972, San Fernando rupture mechanism and the Pacoima strong motion record, Bull. Seism. Soc. Am., 63.
- Booker, A. and Mitronovas, W., 1964, An application of statistical discrimination to classify seismic events, Bull. Seism. Soc. Am., 54, 961-971.
- Boore, D. M., Aki, K. and Todd, T., 1971, A two-dimensional moving dislocation model for a strike-slip fault, Bull. Seism. Soc. Am., 61, 177-194.
- Brune, J. N., 1970, Tectonic stress and the spectra of seismic shear waves from earthquakes, J. Geophys. Res., 75, 4996-5009.
- Brune, J. N., 1973, Earthquake modeling by stick-slip along precut surfaces in stressed foam rubber, Bull. Seism. Soc. Am., 63, 2105-2120.

REFERENCES (Continued)

- Bullen, K. E., 1963, An introduction to the Theory of Seismology, Cambridge University Press, Cambridge, 75-77.
- Der, Z., 1973, M_s - m_b characteristics of earthquakes in the Eastern Himalayan regions, Seismic Data Laboratory Report 296, Teledyne Geotech, Alexandria, Virginia.
- Douglas, A., Hudson, J. A. and Blamey, C., 1973a, A quantitative evaluation of seismic signals at teleseismic distances--III computed P and Rayleigh wave seismograms, Geo. J. R. astr. Soc., 28, 385-410.
- Douglas, A., Marshall, P. D., Gibbs, P. G., Young, I. B. and Blamey, C., 1973b, P signal complexity re-examined, Geophys. J. R. astr. Soc., 33, 195-222.
- Evernden, J. F., 1969, Identification of earthquakes and explosions by use of teleseismic data, J. Geophys. Res., 74, 3828-3856.
- Evernden, J. F., Best, W. J., Pomeroy, P. W., McEvelly, T. V., Savino, J. M. and Sykes, L. R., 1971, Discrimination between small-magnitude earthquakes and explosions, J. Geophys. Res., 76, 8042-8055.
- Gilbert, F., 1973, The relative efficiency of earthquakes and explosions in exciting surface waves and body waves, Geophys. J. R. astr. Soc., 33, 487-488.

REFERENCES (Continued)

- Hanks, T. C. and Thatcher, W., 1972, A graphical representation of seismic source parameters, J. Geophys. Res., 77, 4393-4405.
- Hanks, T. C. and Wyss, M., 1972, The use of body wave spectra in the determination of seismic source parameters, Bull. Seism. Soc. Am., 62, 561-589.
- Hanks, T. C., 1974, The faulting mechanism of the San Fernando earthquake, J. Geophys. Res., 79, 1215-1229.
- Haskell, N., 1964, Total energy and energy spectral density of elastic wave radiation from propagating faults, Bull. Seism. Soc. Am., 54, 1811-1841.
- Haskell, N., 1966, Total energy and energy spectral density of elastic wave radiation from propagating faults, Part II. a statistical source model, Bull. Seism. Soc. Am., 56, 125-140.
- Haskell, N., 1967, Analytic approximation for the elastic radiation from a contained underground explosion, J. Geophys. Res., 72, 2583-2588.
- Haskell, N., 1969, Elastic displacements in the near-field of a propagating fault, Bull. Seism. Soc. Am., 59, 865-908.
- Haskell, N. and Thomson, K. C., 1972, Elastodynamic near-field of a finite, propagating tensile fault, Bull. Seism. Soc. Am., 57, 675-698.

REFERENCES (Continued)

- Johnson, T., Wu, F. T. and Scholz, C. H., 1973, Source parameters for stick slip and for earthquakes, *Science*, 179, 278-280.
- Jungels, P. H. and Frazier, G. A., 1973, Finite element analysis of the residual displacements for an earthquake rupture: source parameters for the San Fernando earthquake, *J. Geophys. Res.*, 78, 5062-5083.
- Kamb, B., Silver, L. T., Abrams, M., Carter, B., Jordan, T. and Minster, B., 1971, Pattern of faulting and nature of fault movement in the San Fernando earthquake, *U. S. Geol. Sur. Prof. Pap.*, 733, 41-54.
- Lacoss, R. T., 1969, LASA decision probabilities for M_s - m_b and modified spectral ratio, Lincoln Laboratory Technical Report 23 July.
- Landers, T., 1972, Some interesting Central Asian events on the $M_s:m_b$ diagram, *Geophys. J. R. astr. Soc.*, 31, 329-339.
- Manchee, E. B., 1972, Short period seismic discrimination, *Nature*, 239, 152-153.
- Mansinha, L., 1964, The velocity of shear fracture, *Bull. Seism. Soc. Am.*, 50, 396-376.

REFERENCES (Continued)

- Marshall, P. D. and Basham, P. W., 1972, Discrimination between earthquakes and underground explosions employing an improved M_s scale, *Geophys. J. R. astr. Soc.*, 28, 431-458.
- Minster, J. B., 1973, *Elastodynamics of Failure in a Continuum*, Thesis, California Institute of Technology.
- Mikumo, T., 1973, Faulting process of the San Fernando earthquake of February 9, 1971, inferred from static and dynamic near-field displacements, *Bull. Seism. Soc. Am.*, 63, 249-268.
- Molnar, P. and Wyss, M., 1972, Moments, source dimensions and stress drops of shallow-focus earthquakes in the Tonga-Kermadec arc, *Phys. Earth Planet. Int.*, 6, 263-278.
- Molnar, P., Tucker, B. E. and Brune, J. N., 1973, Corner frequencies of P and S waves and models of earthquake sources, *Bull. Seism. Soc. Am.*, 63, 2091-2104.
- Murray, G. F., 1973, Dislocation mechanism--the Parkfield 1966 accelerograms, *Bull. Seism. Soc. Am.*, 63, 1539-1556.
- Randall, M. J., 1966, Seismic radiation from a sudden phase transition, *J. Geophys. Res.*, 71, 5297-5302.
- Ringdal, F. and Whitelaw, R. L., 1973, Continued evaluation of the Norwegian short-period array, Special Report No. 9, Texas Instruments.

REFERENCES (Continued)

- Savage, J. C., 1966, Radiation from a realistic model of faulting, Bull. Seism. Soc. Am., 56, 577-592.
- Savage, J. C., 1972, The relation of corner frequency to fault dimensions, J. Geophys. Res., 77, 3788-3795.
- Savage, J. C., 1974, Relation between P and S wave corner frequencies in the seismic spectrum (in press).
- Thatcher, W., 1972, Regional variations of seismic source parameters in the northern Baja California area, Bull. Seism. Soc. Am., 77, 1549-1565.
- Thatcher, W. and Hanks, T. C., 1973, Source parameters of Southern California earthquakes, J. Geophys. Res., 78, 8547-8576.
- Trifunac, M. D. and Brune, J. N., 1970, Complexity of energy release from the Imperial Valley, California earthquake of 1940, Bull. Seism. Soc. Am., 60, 137-160.
- Trifunac, M. D., 1972, Stress estimates for the San Fernando, California earthquake of February 9, 1971: Main event and thirteen aftershocks, Bull. Seism. Soc. Am., 62, 721-750.

REFERENCES (Continued)

- Tucker, B. E. and Brune, J. N., 1973, Seismograms, S wave spectra, and source parameters for after-shocks of the San Fernando earthquake of February 9, 1971 in Geological and Geophysical Studies, Vol. 3, San Fernando Earthquake of February 9, 1971, NOAA, U. S. Dept. of Commer., Washington, D. C.
- von Seggern, D. H. and Blandford, R. R., 1972, Source time functions and spectra for underground nuclear explosions, Geophys. J. R. astr. Soc., 31, 83-97.
- Weertman, J., 1969, Dislocation motion on an interface with friction that is dependent on sliding velocity, J. Geophys. Res., 74, 6617-6627.
- Werth, G. C. and Herbst, R. F., 1963, Comparison of amplitudes of seismic waves from nuclear explosions in four mediums, J. Geophys. Res., 68, 1463-1475.
- Wyss, M. and Brune, J. N., 1967, The Alaska earthquake of 28 March 1964: a complex multiple rupture, Bull. Seism. Soc. Am., 57, 1017-1023.
- Wyss, M., 1970, Stress estimates of South American shallow and deep earthquakes, J. Geophys. Res., 75, 1529-1544.
- Wyss, M., Hanks, T. C. and Liebermann, R. C., 1971, Comparison of P wave spectra of underground explosions and earthquakes, J. Geophys. Res., 76, 2715-2729.

REFERENCES (Continued)

- Wyss, M. and Brune, J., 1971, Regional variations of source properties in Southern California estimated from the ratio of short- to long-period amplitudes, Bull. Seism. Soc. Am., 61, 1153-1167.
- Wyss, M. and Molnar, P., 1972, Source parameters of intermediate and deep focus earthquakes in the Tonga arc, Phys. Earth Planet. Int., 6, 279-292.
- Wyss, M. and Hanks, T. C., 1972, The source parameters of the San Fernando earthquake inferred from teleseismic body waves, Bull. Seism. Soc. Am., 62, 591-602.

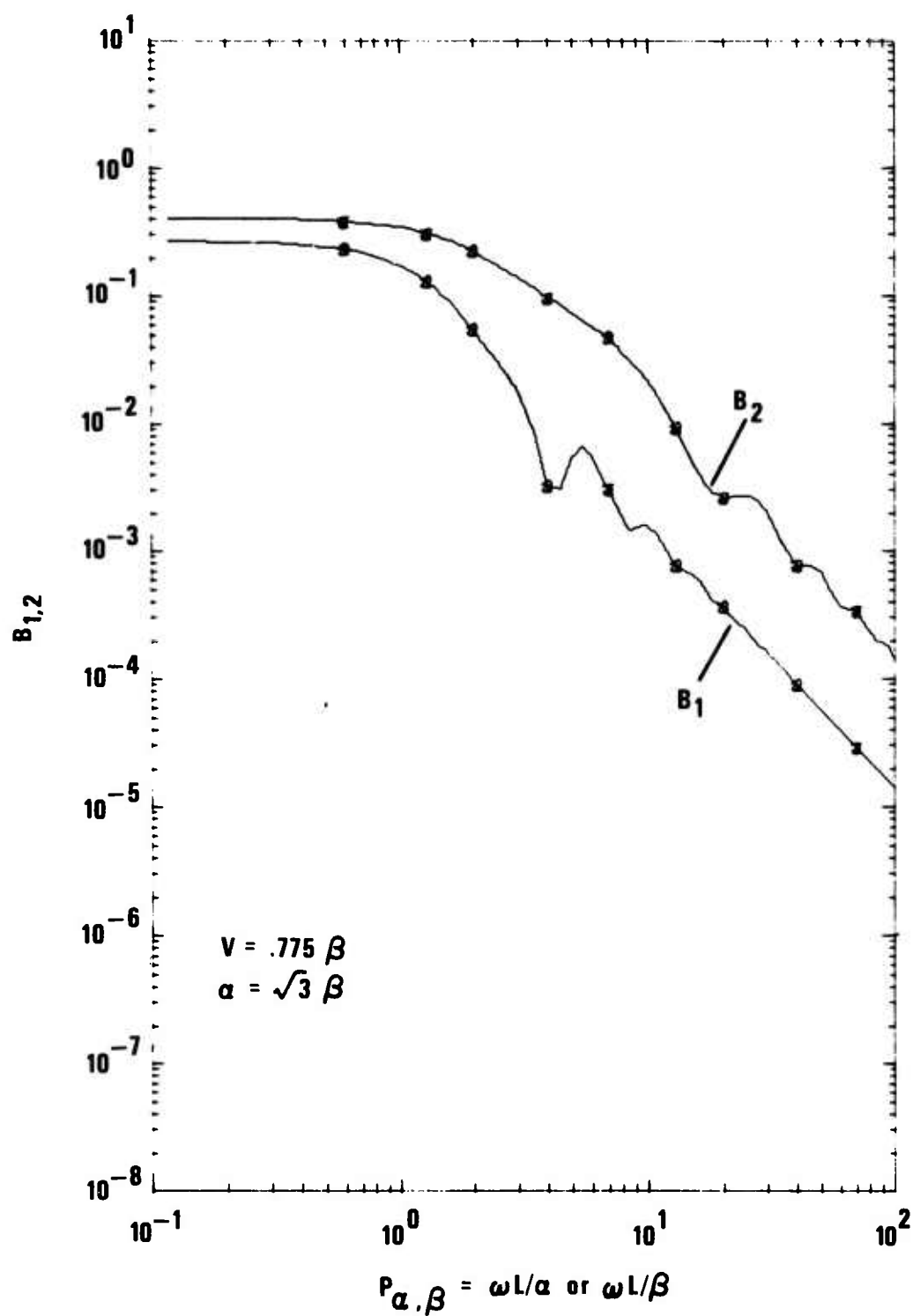


Figure 1. B functions for a slip earthquake with slip in direction of fault propagation. Curves are the same as those plotted by Haskell (1964).

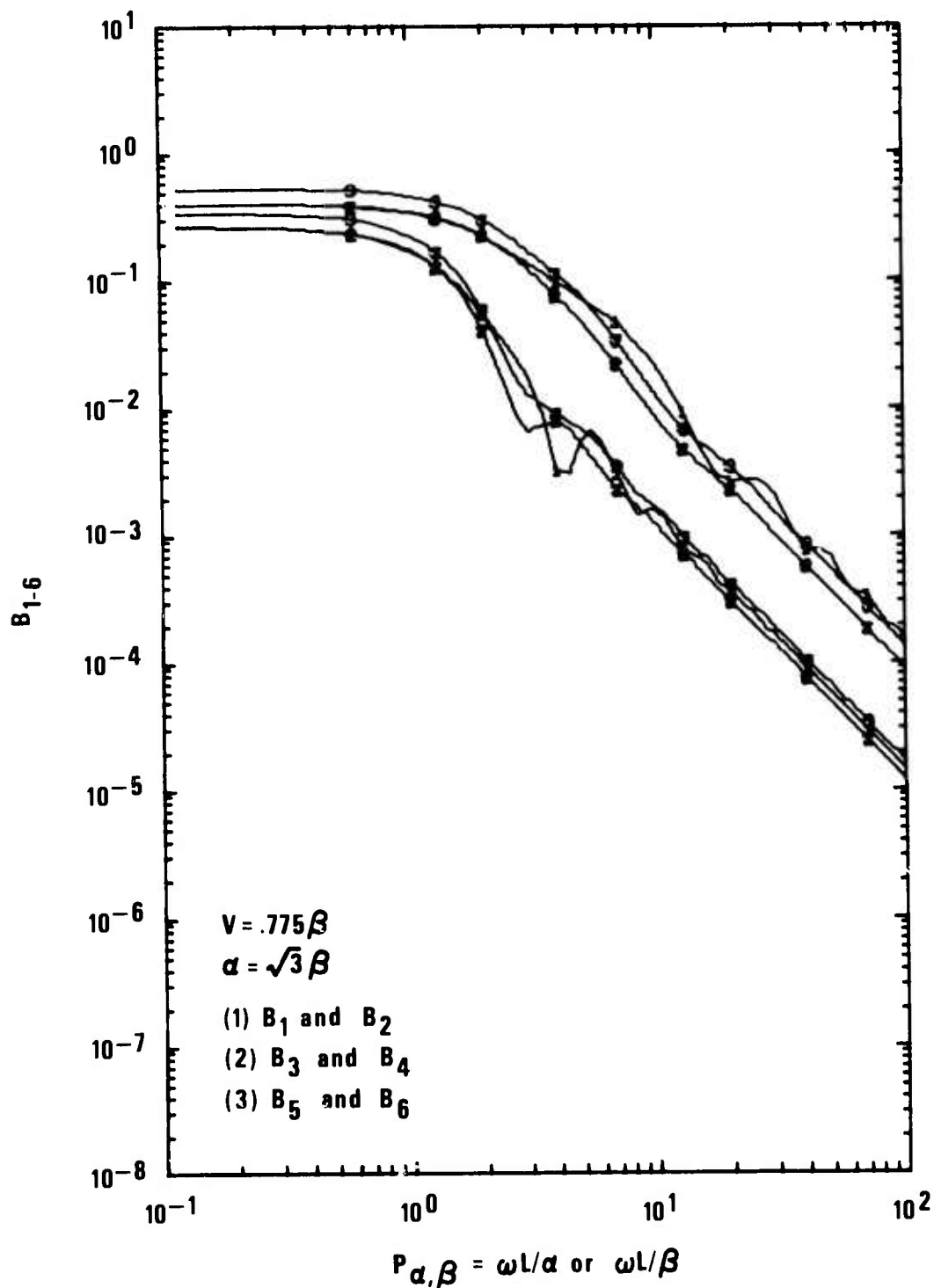


Figure 2. B functions for all three types of fault motion considered by Haskell (1964). Plotted from formulas given by Haskell.

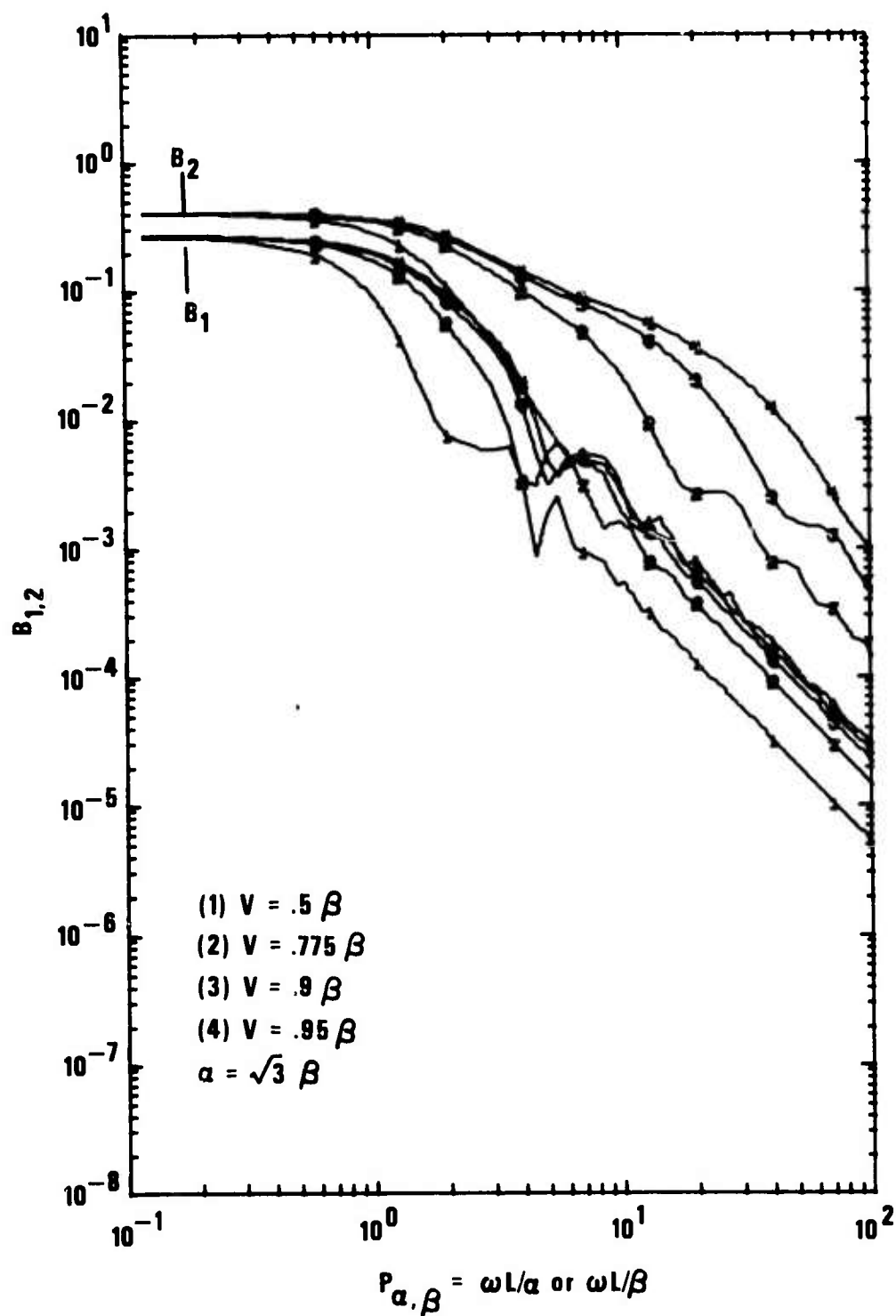


Figure 3. Variations in amplitude as a function of propagation velocity for the B functions for a slip earthquake with slip in direction of fault propagation. Intermediate slope of ω^{-1} can be seen at high velocities for the shear (B_2) functions.

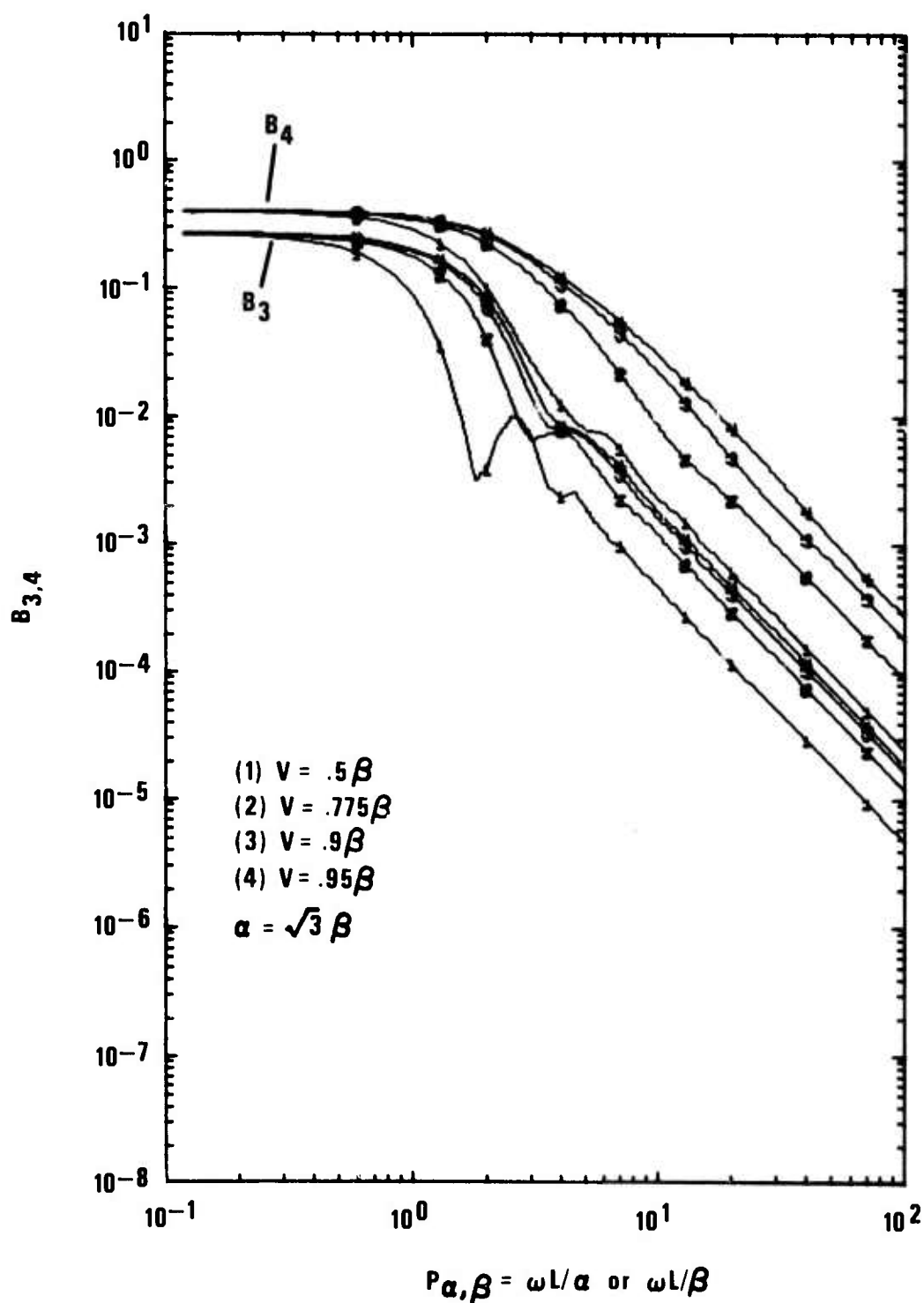


Figure 4. Variations in amplitude as a function of propagation velocity for the B functions for a slip earthquake with slip in fault plane and perpendicular to direction of fault propagation. Intermediate slope is not so apparent as in Figure 3.

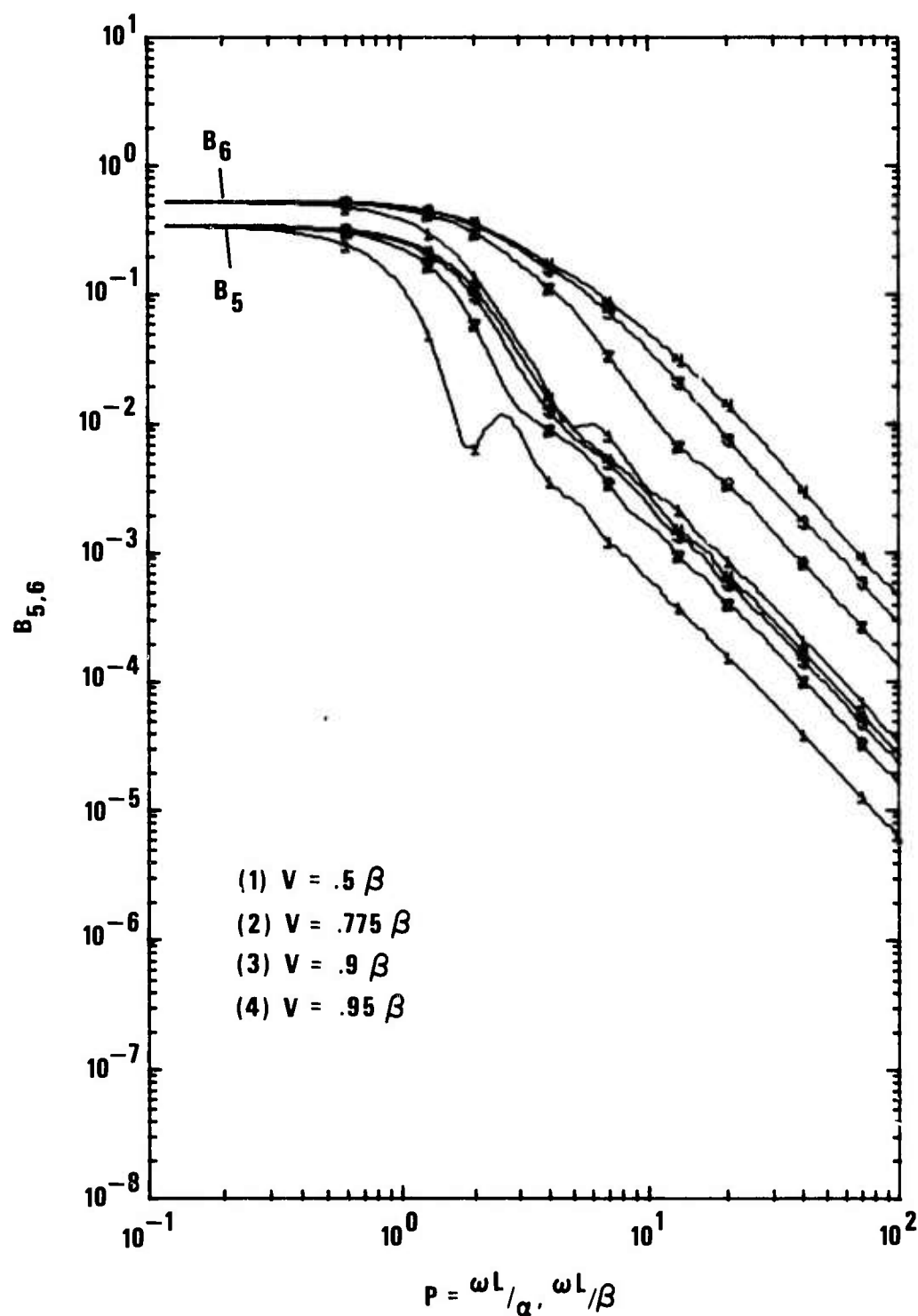


Figure 5. Variations in amplitude as a function of propagation velocity for the B functions for a tensional earthquake. Intermediate slope is not so apparent as in Figure 3.

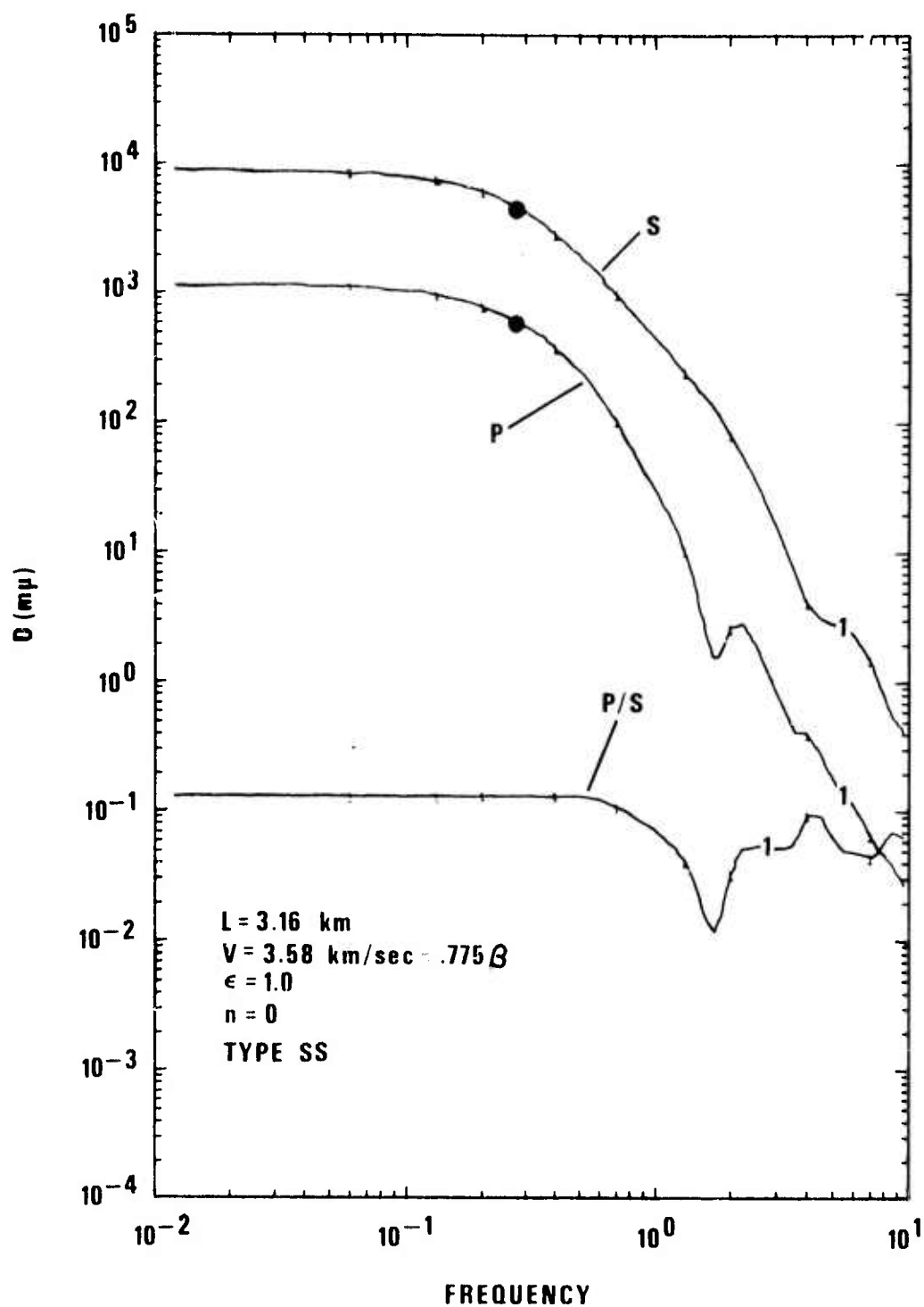


Figure 6. S and P displacement amplitude spectra and their ratio for a simple earthquake.

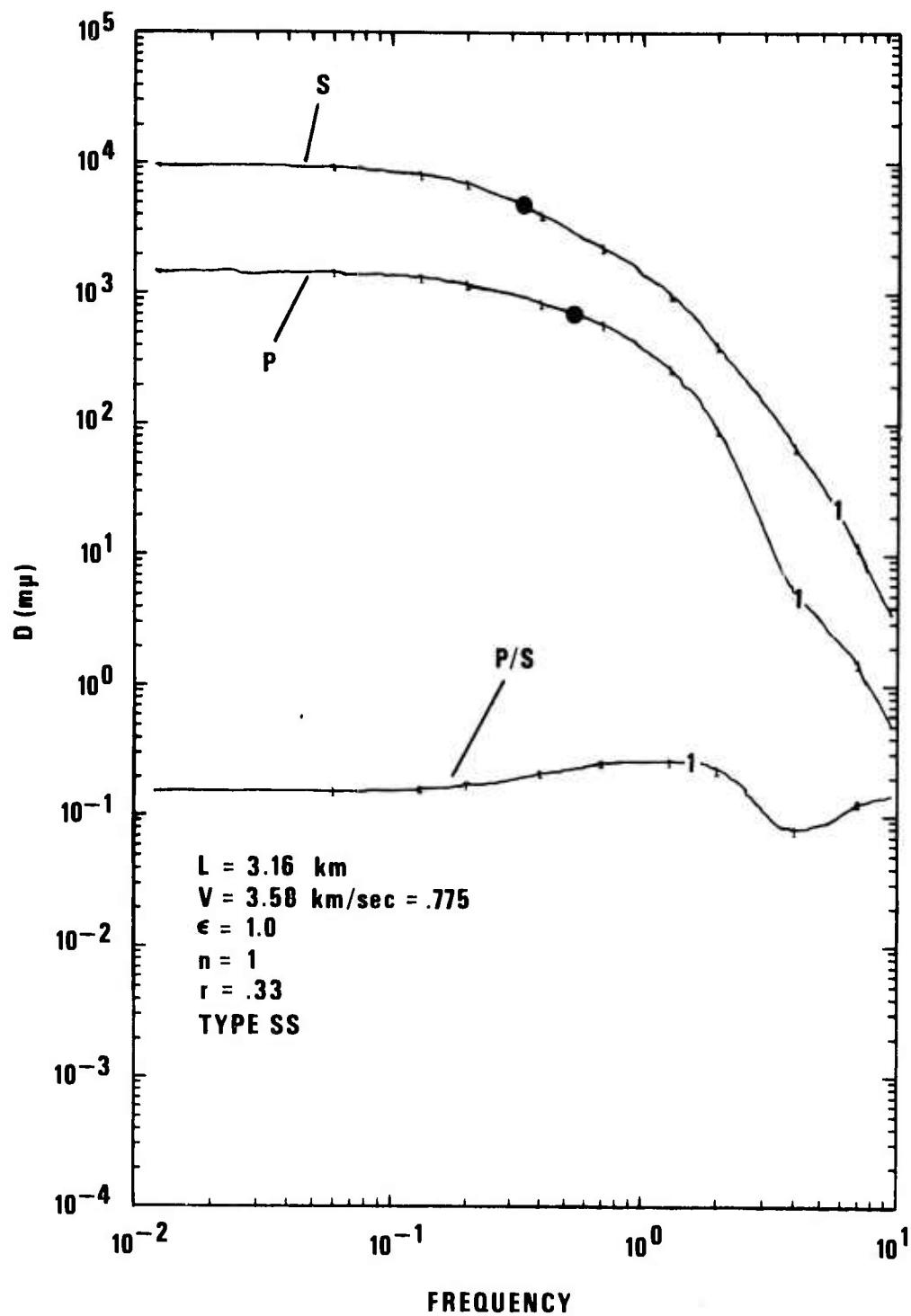


Figure 7. S and P displacement amplitude spectra and their ratio for a simple earthquake, plus one sublevel.

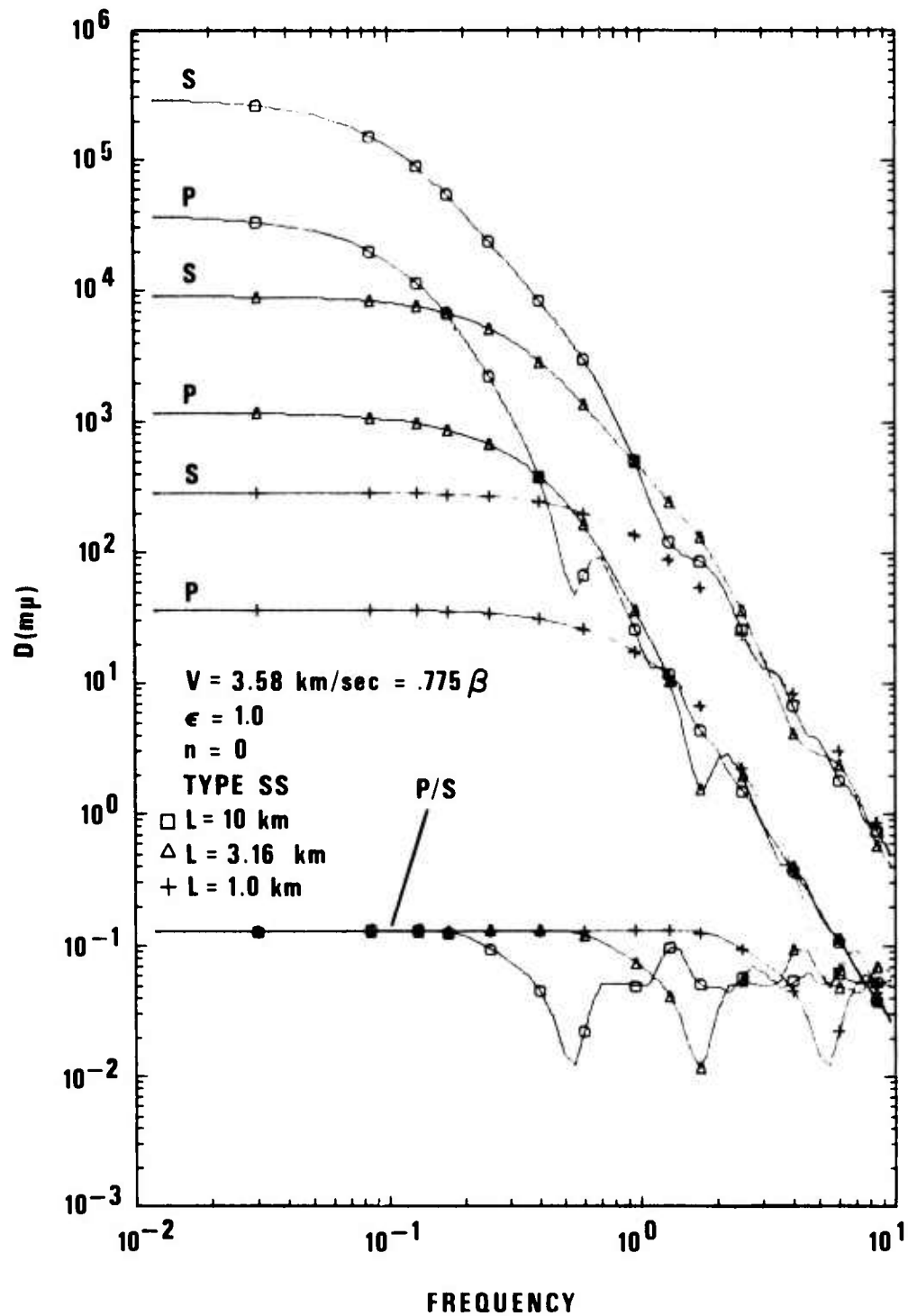


Figure 8. S and P displacement amplitude spectra and their ratio for three simple earthquakes of different sizes. Note the convergence of amplitude at high frequencies; and the "periodic" behavior of the ratios.

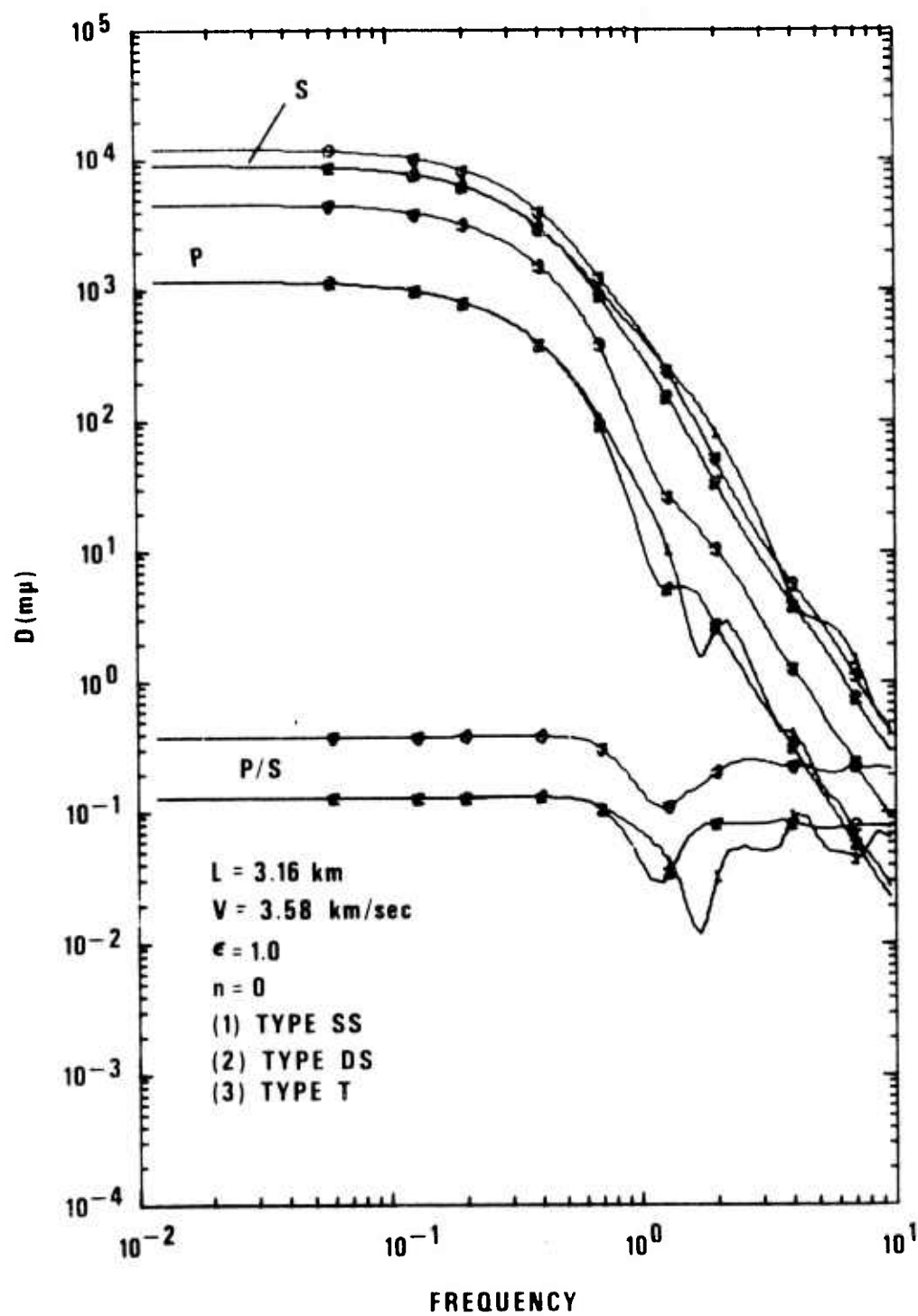


Figure 9. S and P displacement amplitude spectra and their ratio for three types of simple earthquakes.

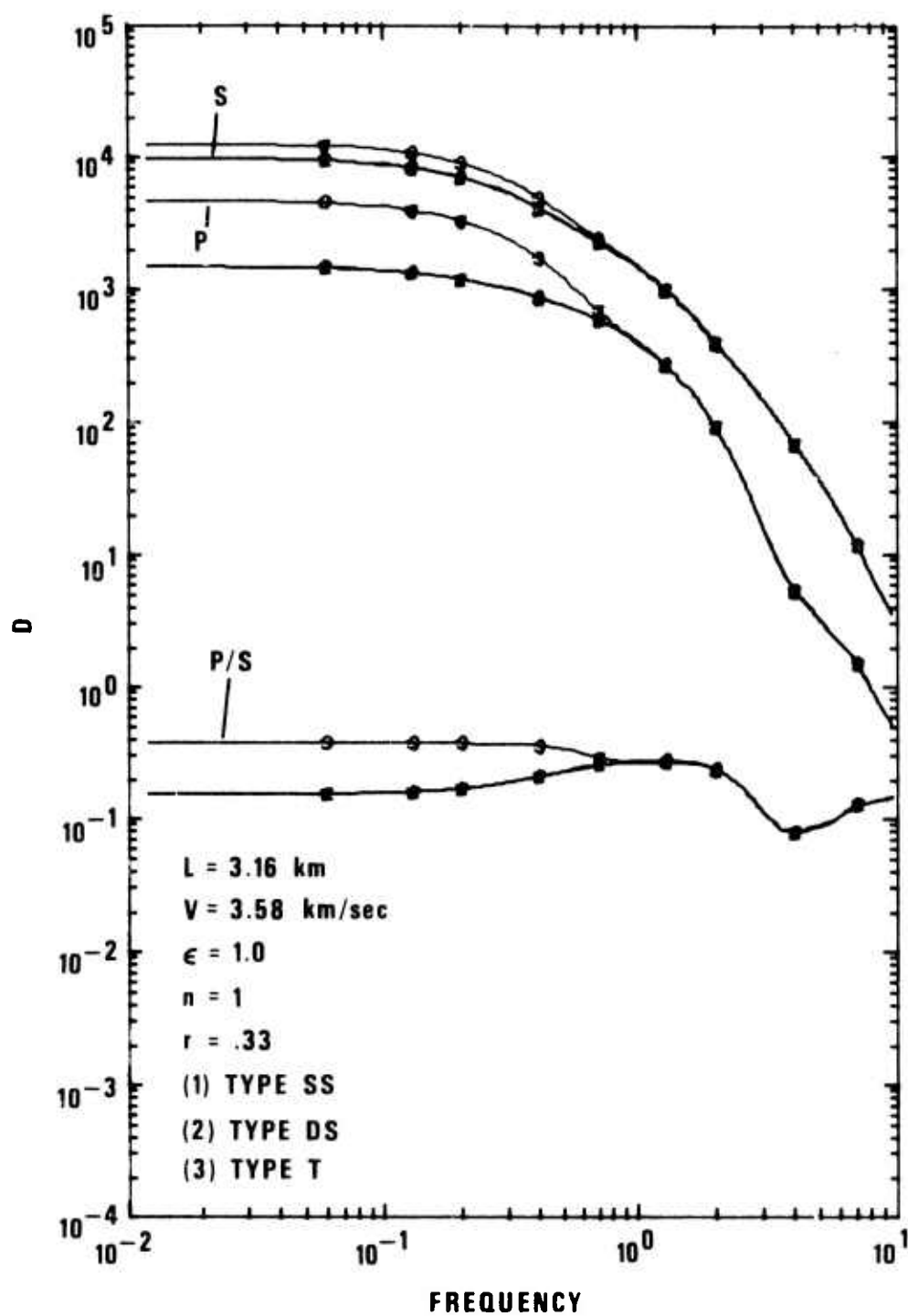


Figure 10. S and P displacement amplitude spectra and their ratio for three types of simple earthquake, plus one sublevel.

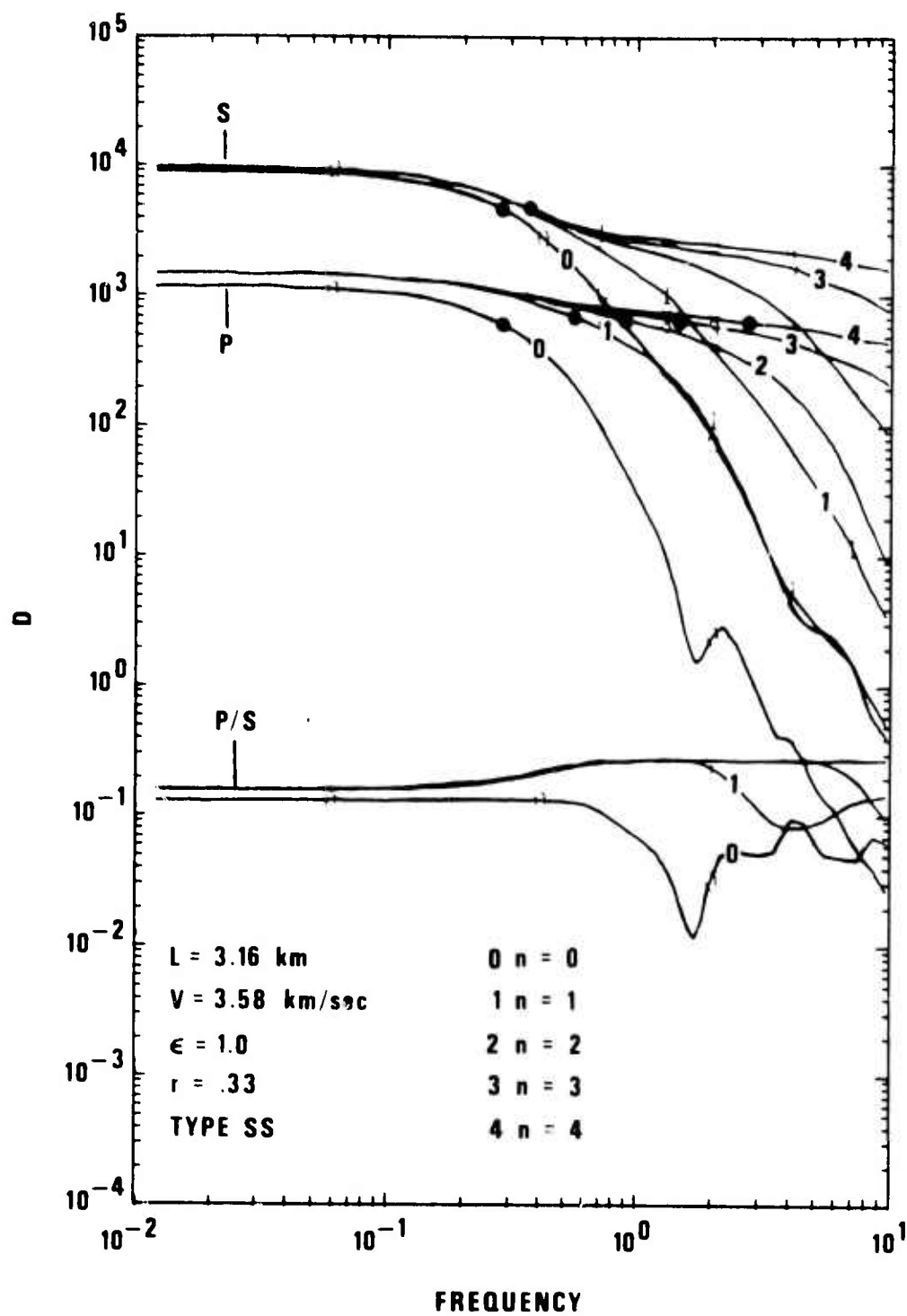


Figure 11. S and P displacement amplitude spectra and their ratio for a simple earthquake plus 0, 1, 2, 3, or 4 sublevels.

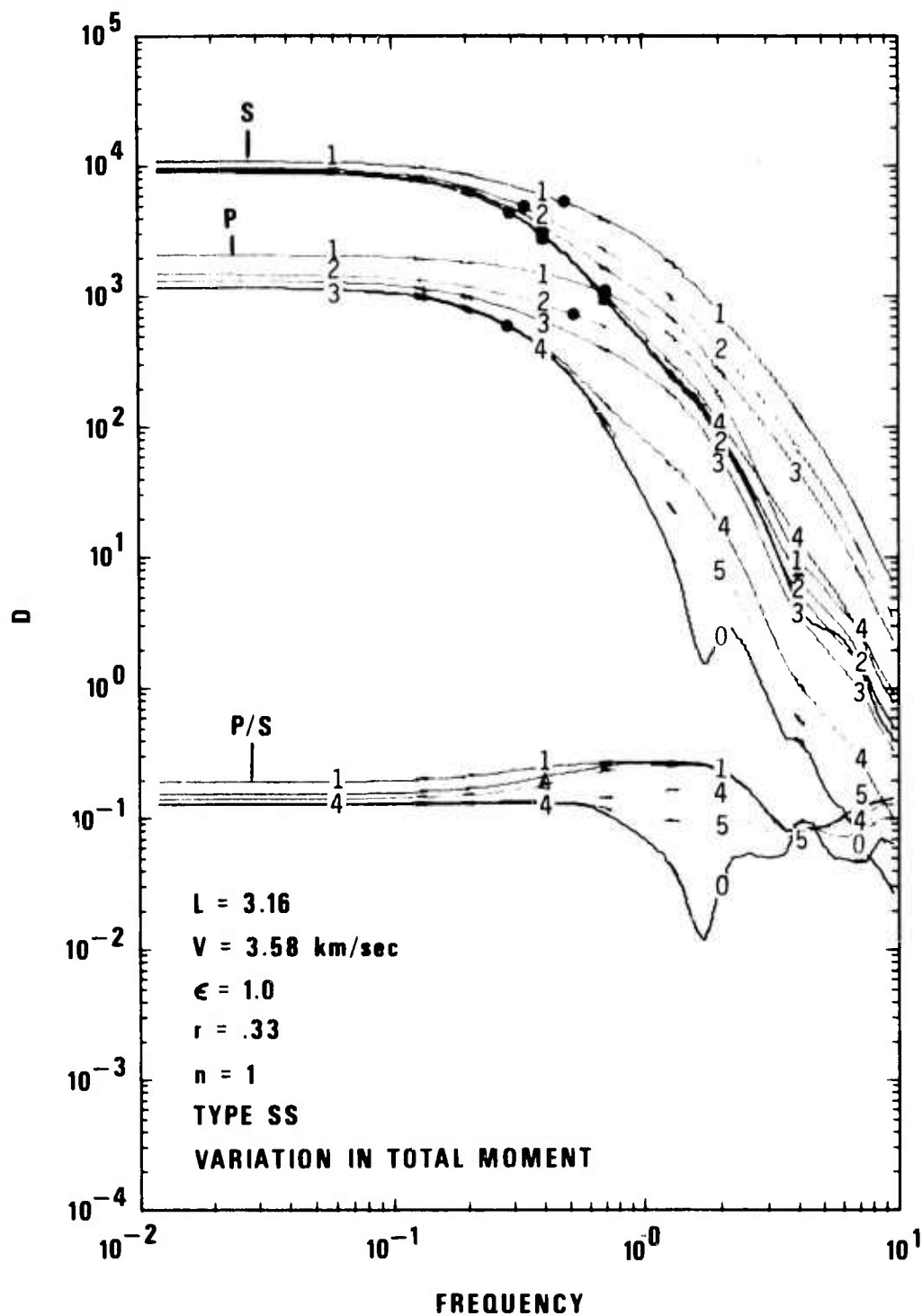


Figure 12. S and P displacement amplitude spectra and their ratio for a simple earthquake plus one sublevel with a range of submoments.

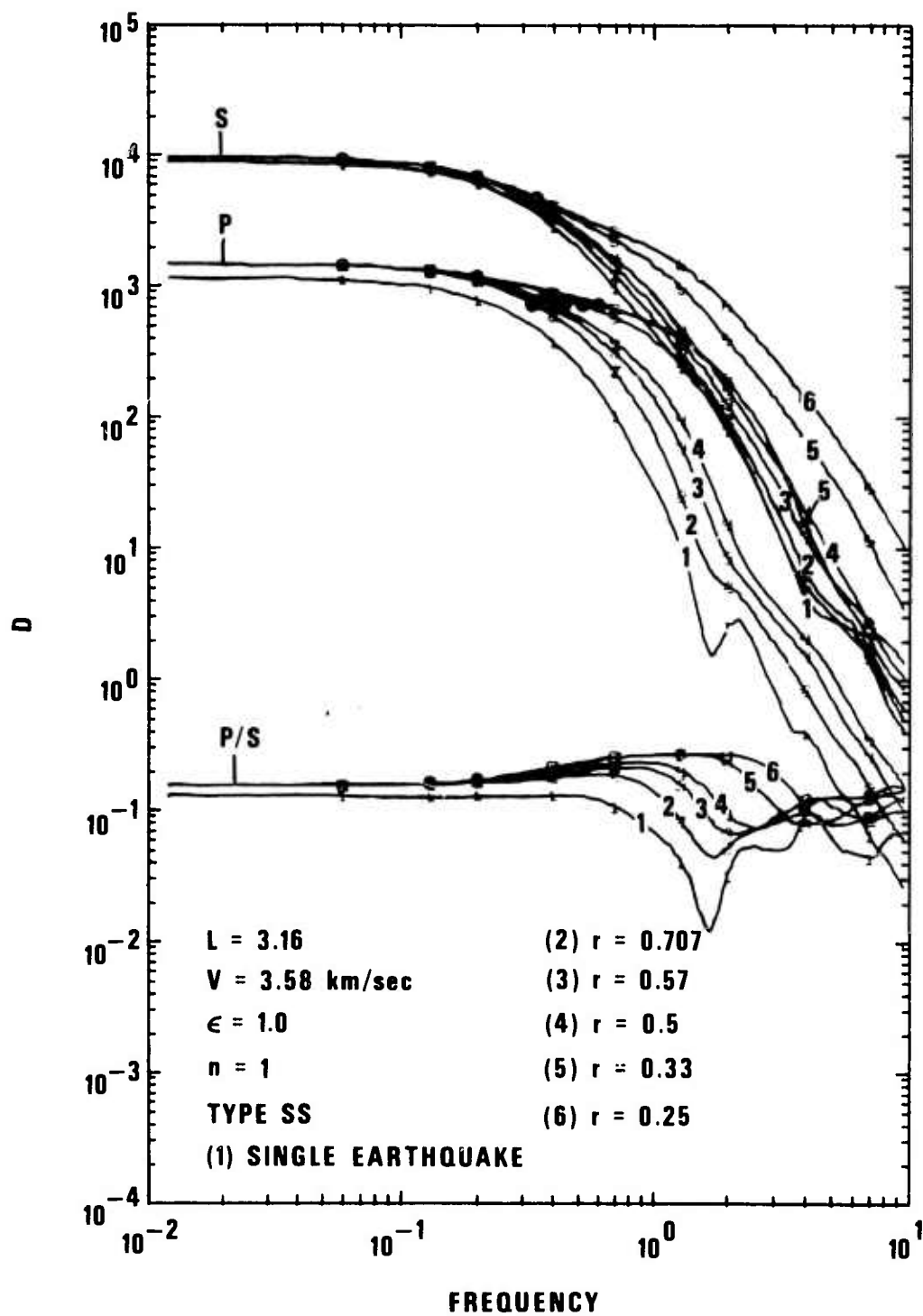


Figure 13. S and P displacement amplitude spectra and their ratio for a simple earthquake plus one sublevel with a range of earthquake sizes but constant total moment.

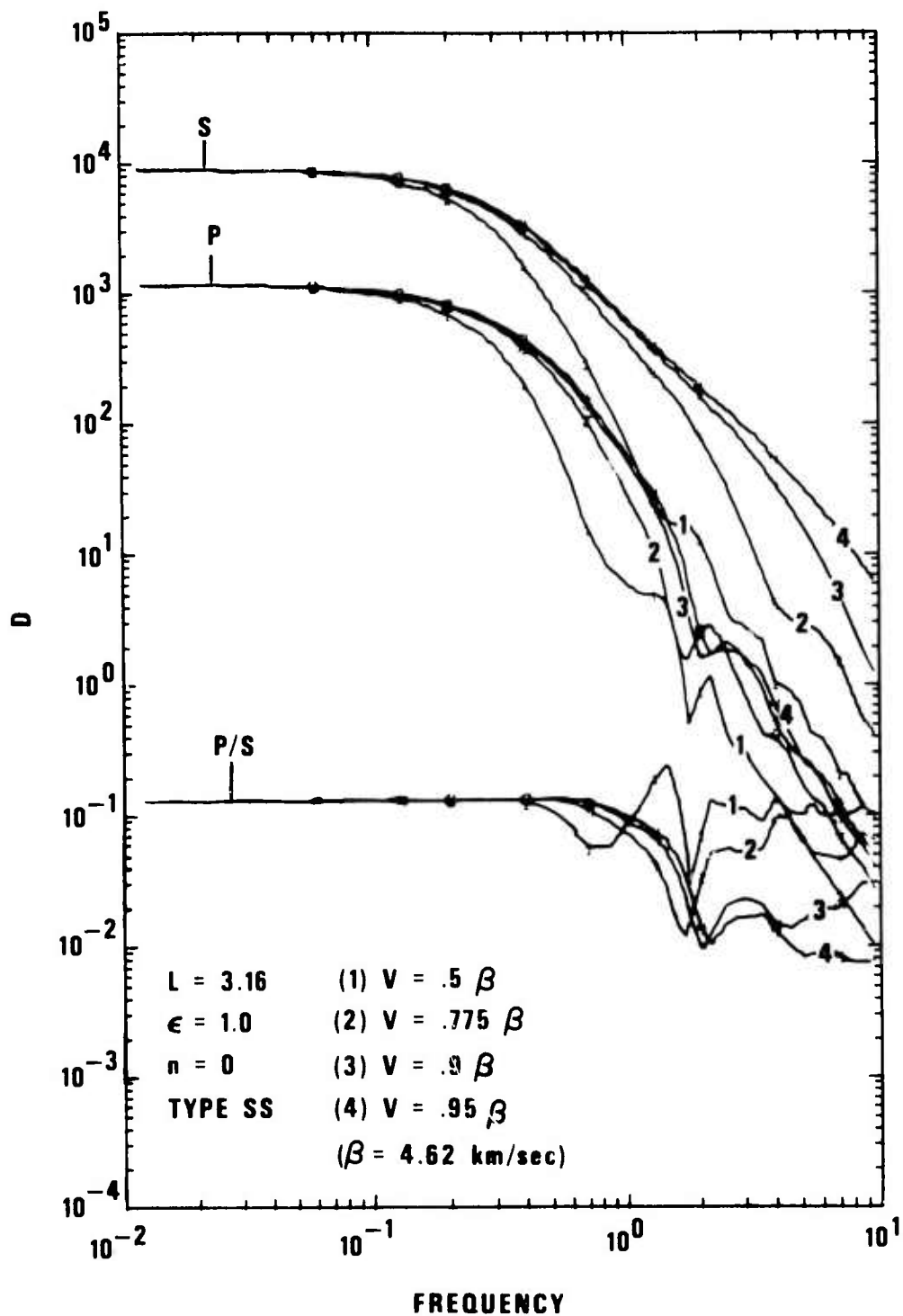


Figure 14. S and P displacement amplitude spectra and their ratio for a simple earthquake and with a range of propagation velocities.

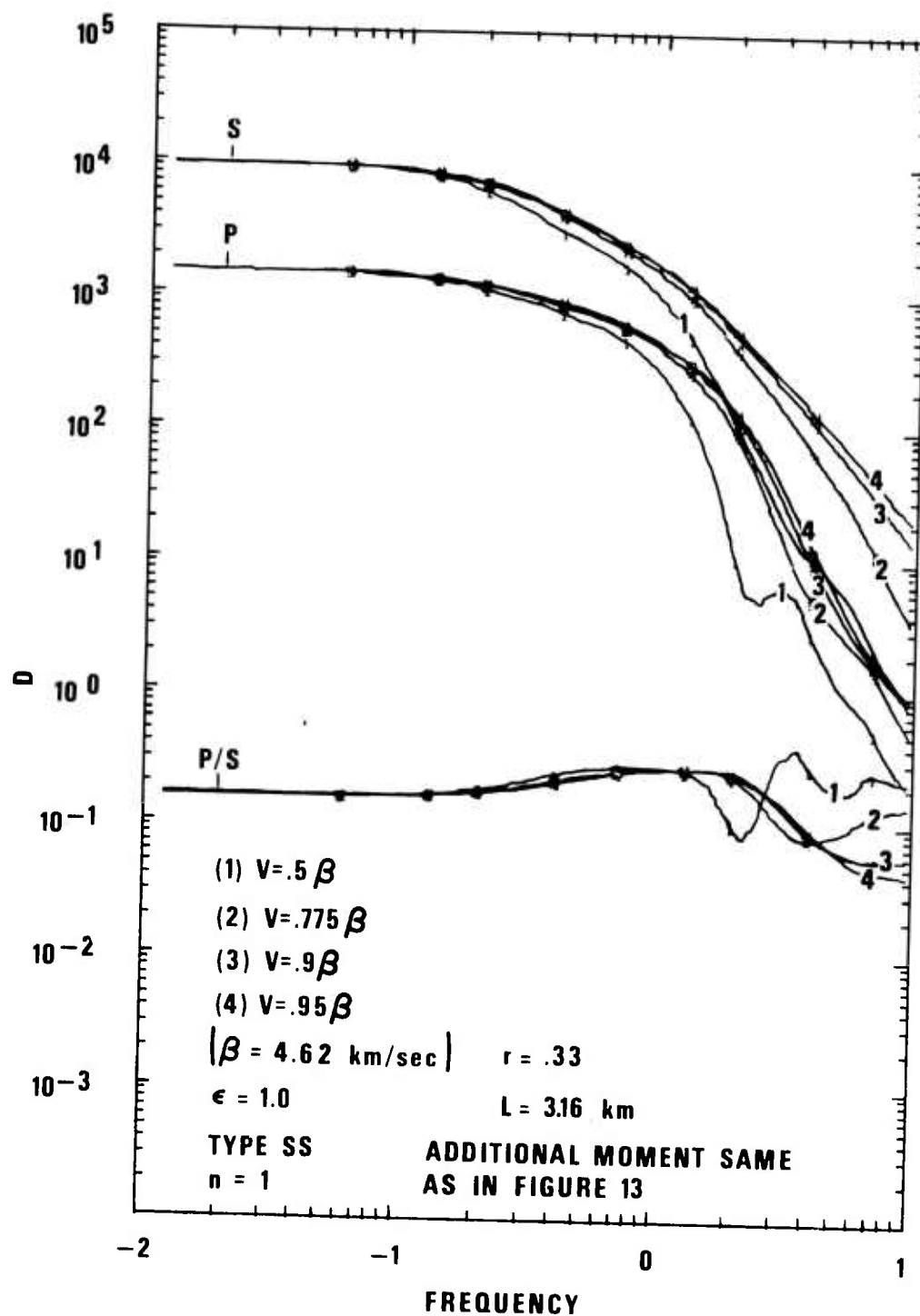


Figure 15. S and P displacement amplitude spectra and their ratio for a simple earthquake, plus one sublevel, for a range propagation velocities.

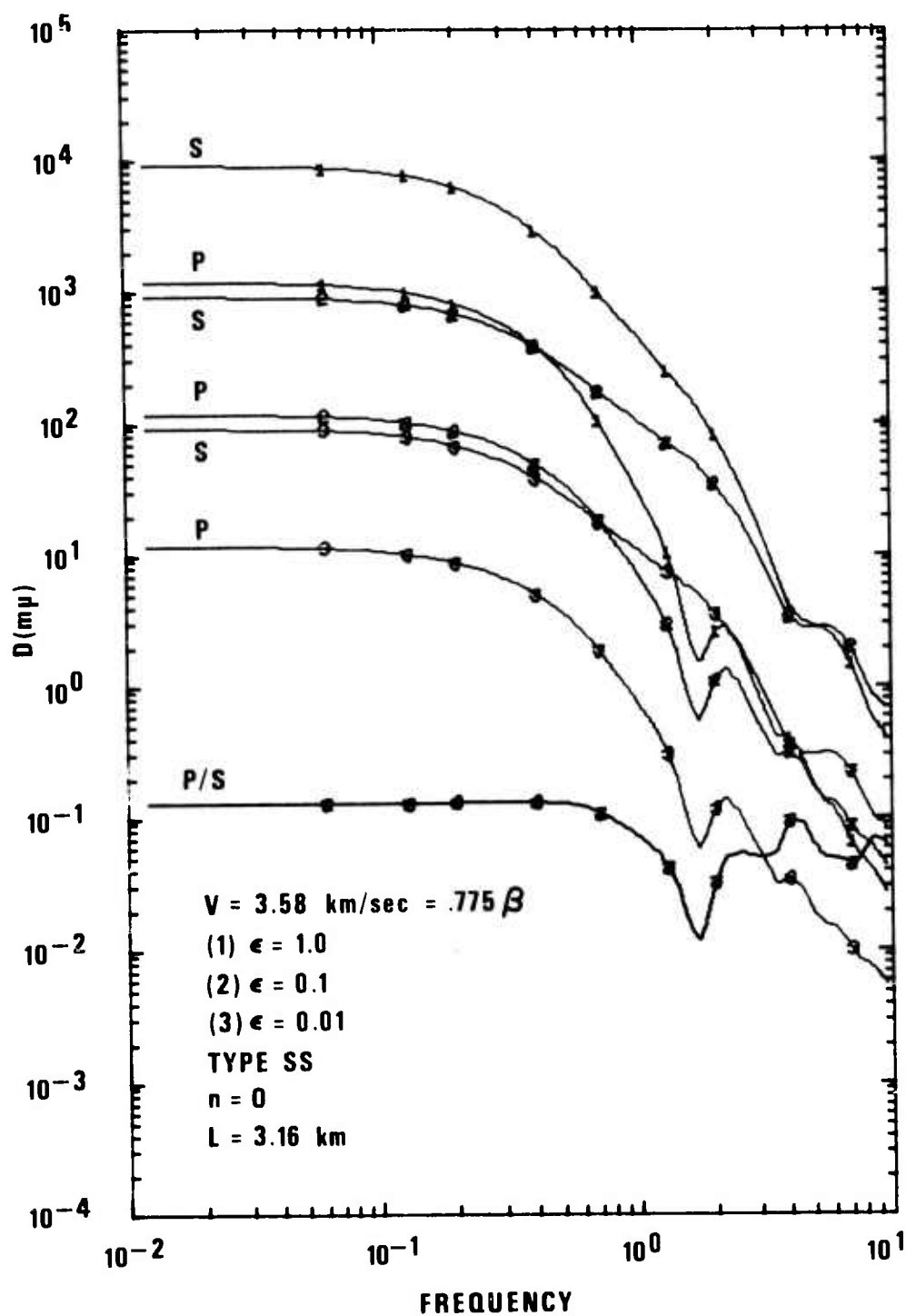


Figure 16. S and P displacement amplitude spectra and their ratio for a simple earthquake and with a range of fractional stress drops. An intermediate slope of ω^{-1} can be seen.

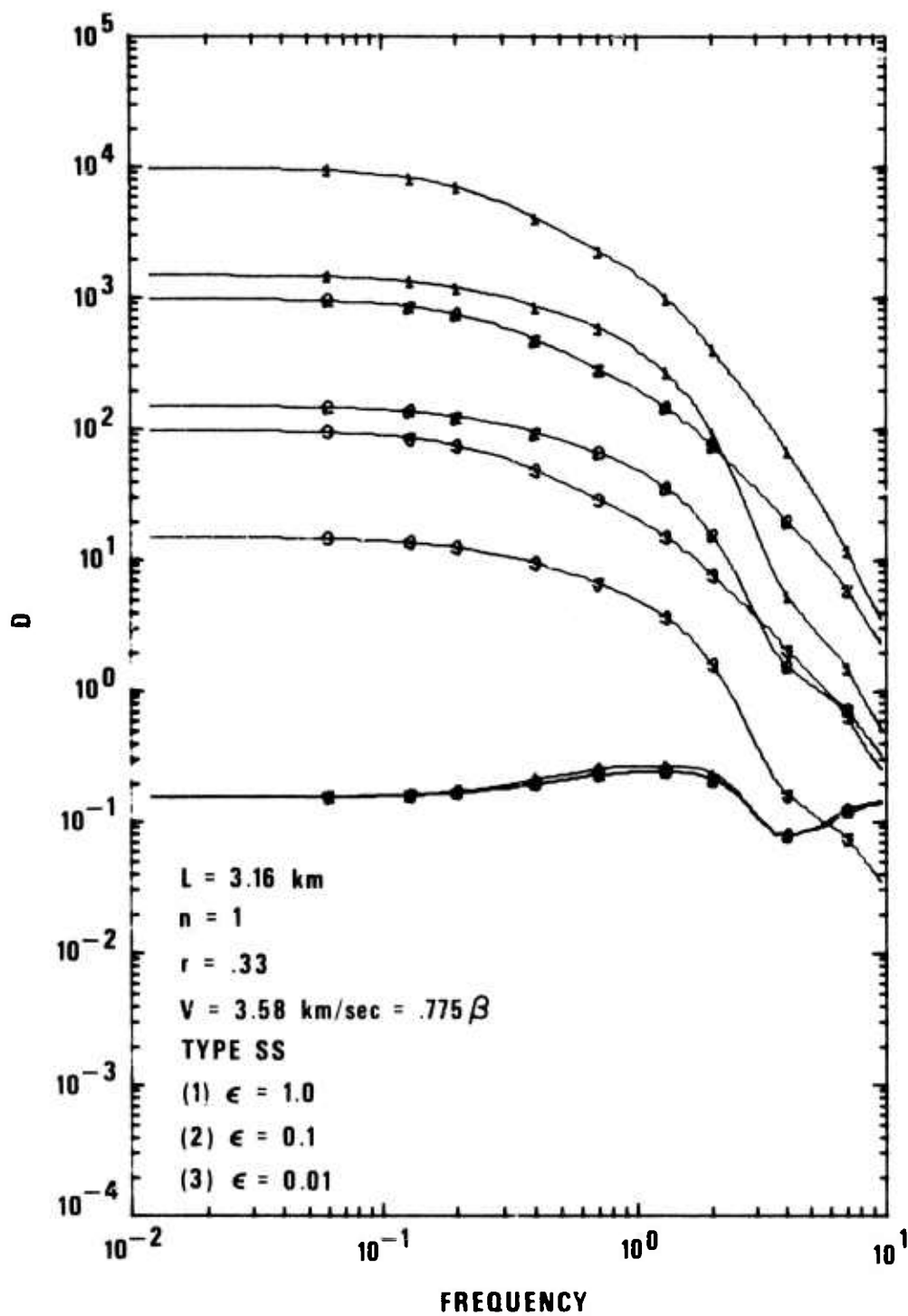


Figure 17. S and P displacement amplitude spectra and their ratio for a simple earthquake plus one sublevel for a range of fractional stress drops.

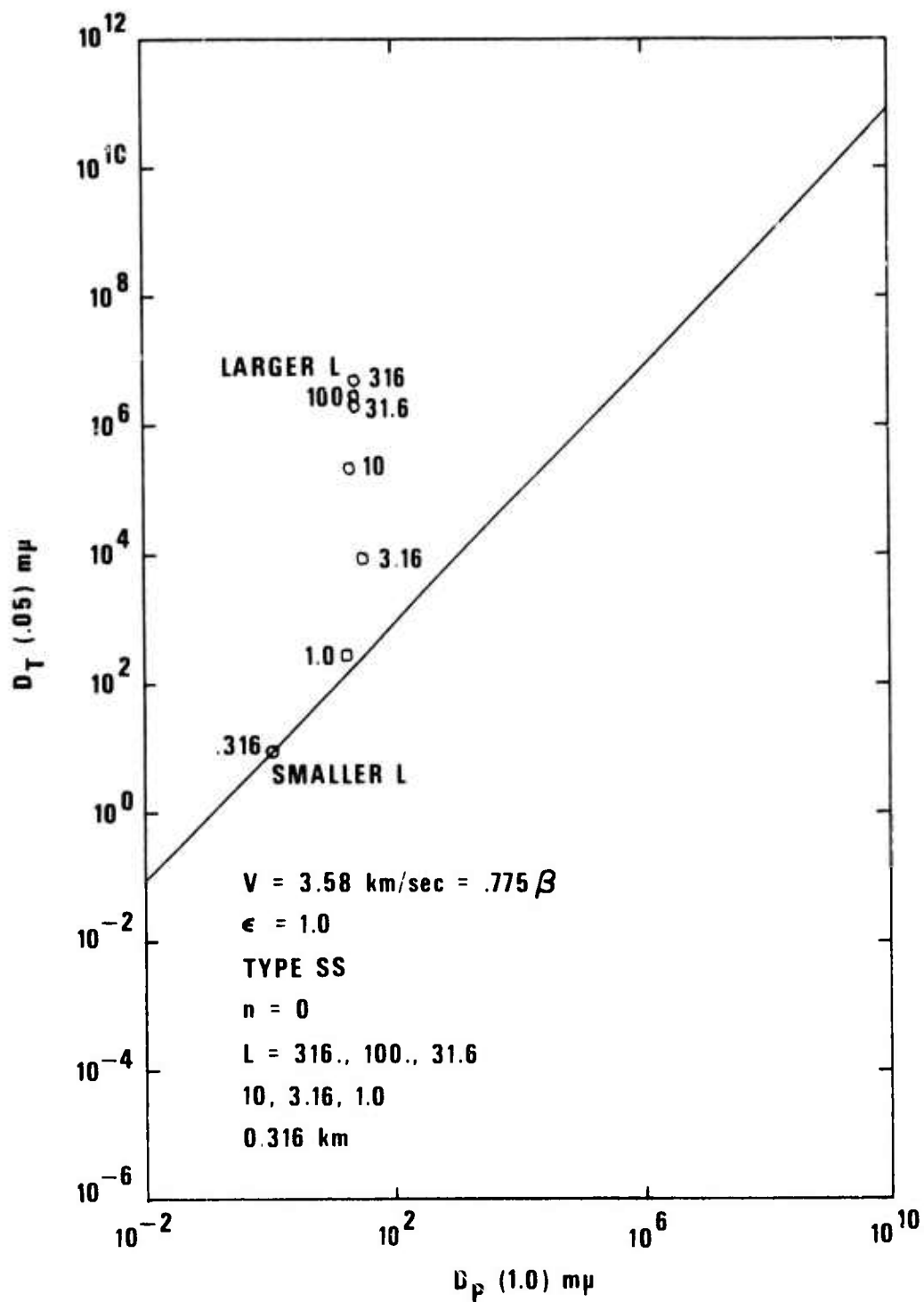


Figure 18. 20-second total displacement versus 1-second compressional displacement for simple earthquakes for a range of lengths.

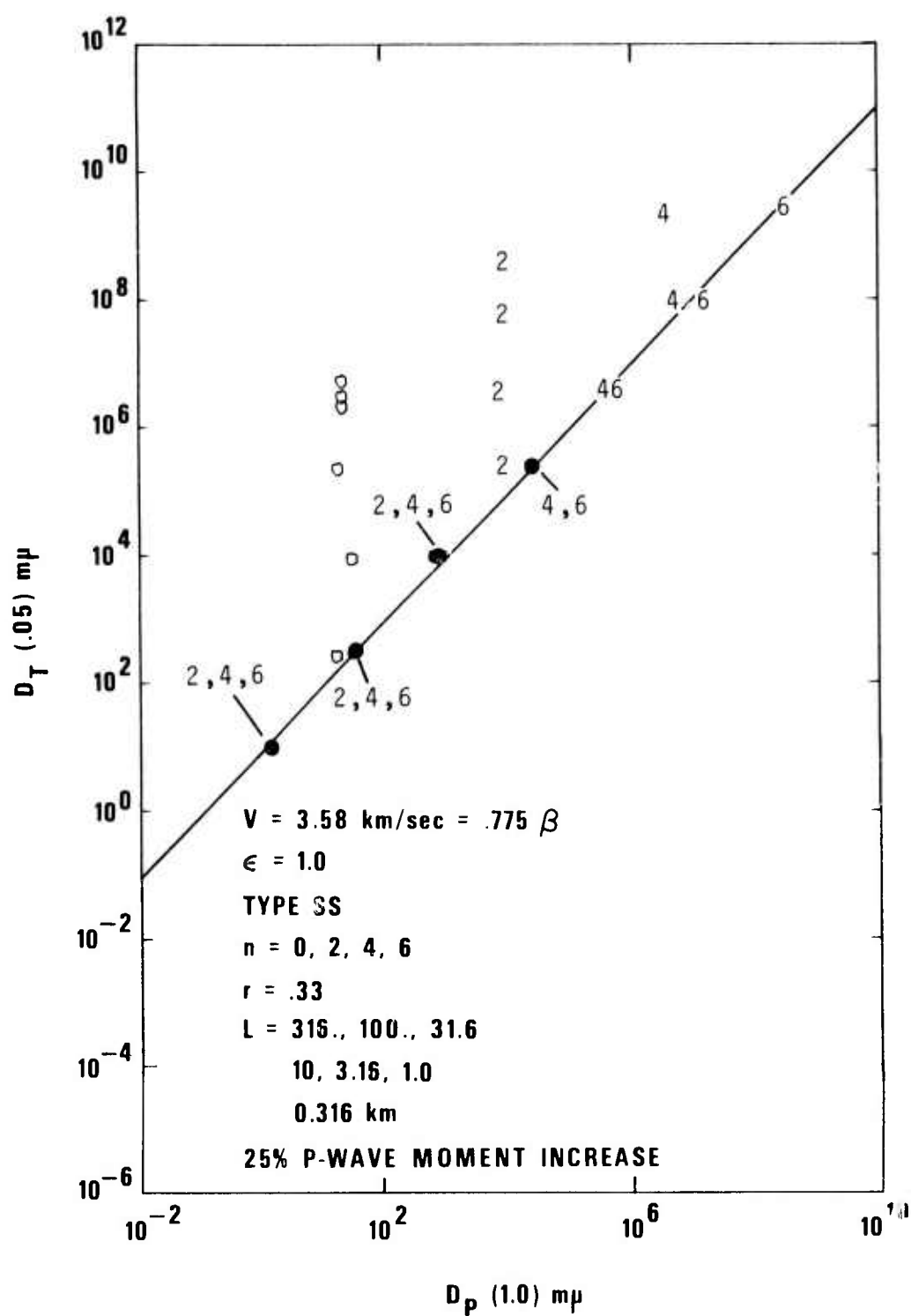


Figure 19. 20-second total displacement versus 1-second compressional displacement for simple earthquakes for a range of lengths plus 0, 2, 4 or 6 sublevels with constant total moment leading to an increase of 25%. Ratio of subearthquake lengths $r = 0.33$.

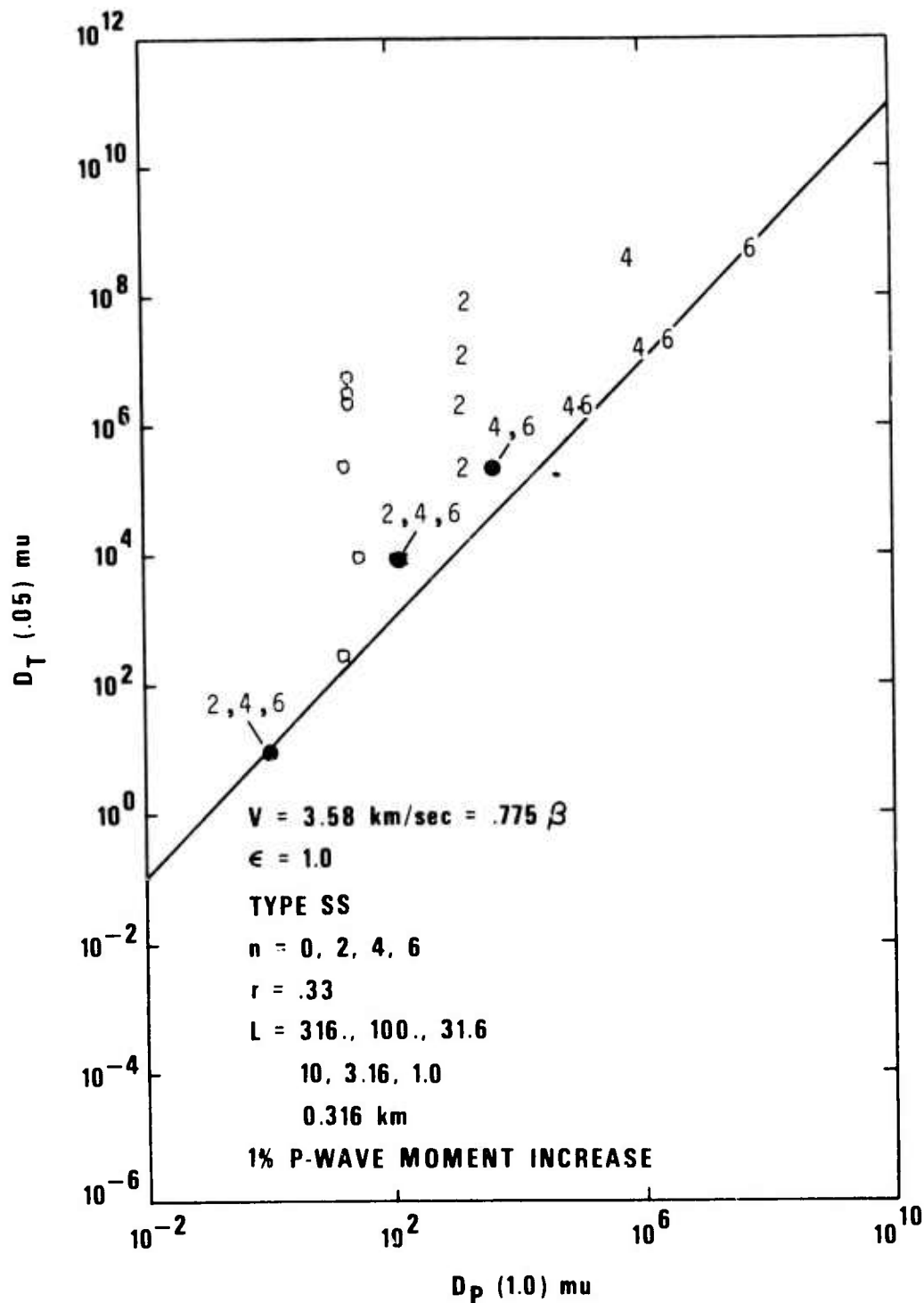


Figure 20. 20-second total displacement versus 1-second compressional displacement for simple earthquakes for a range of lengths, plus 0, 2, 4 or 6 sublevels with constant total moment leading to an increase of 1%. Ratio of subearthquake lengths $r = 0.33$.

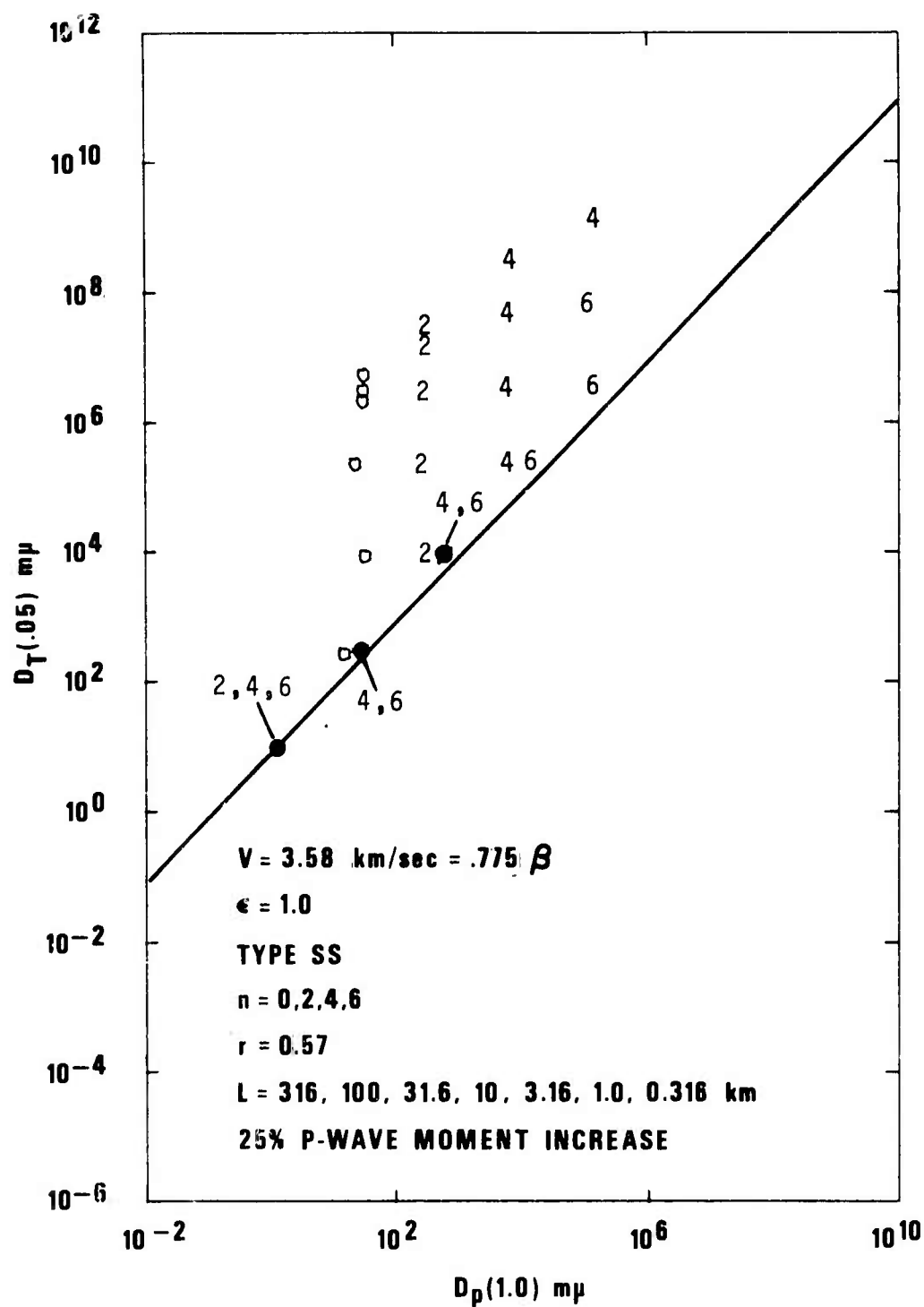


Figure 21. 20-second total displacement versus 1-second compressional displacement for simple earthquakes for a range of lengths plus 0, 2, 4 or 6 sublevels with constant total moment leading to an increase of 25%. Ratio of subearthquake lengths $r = 0.57$.

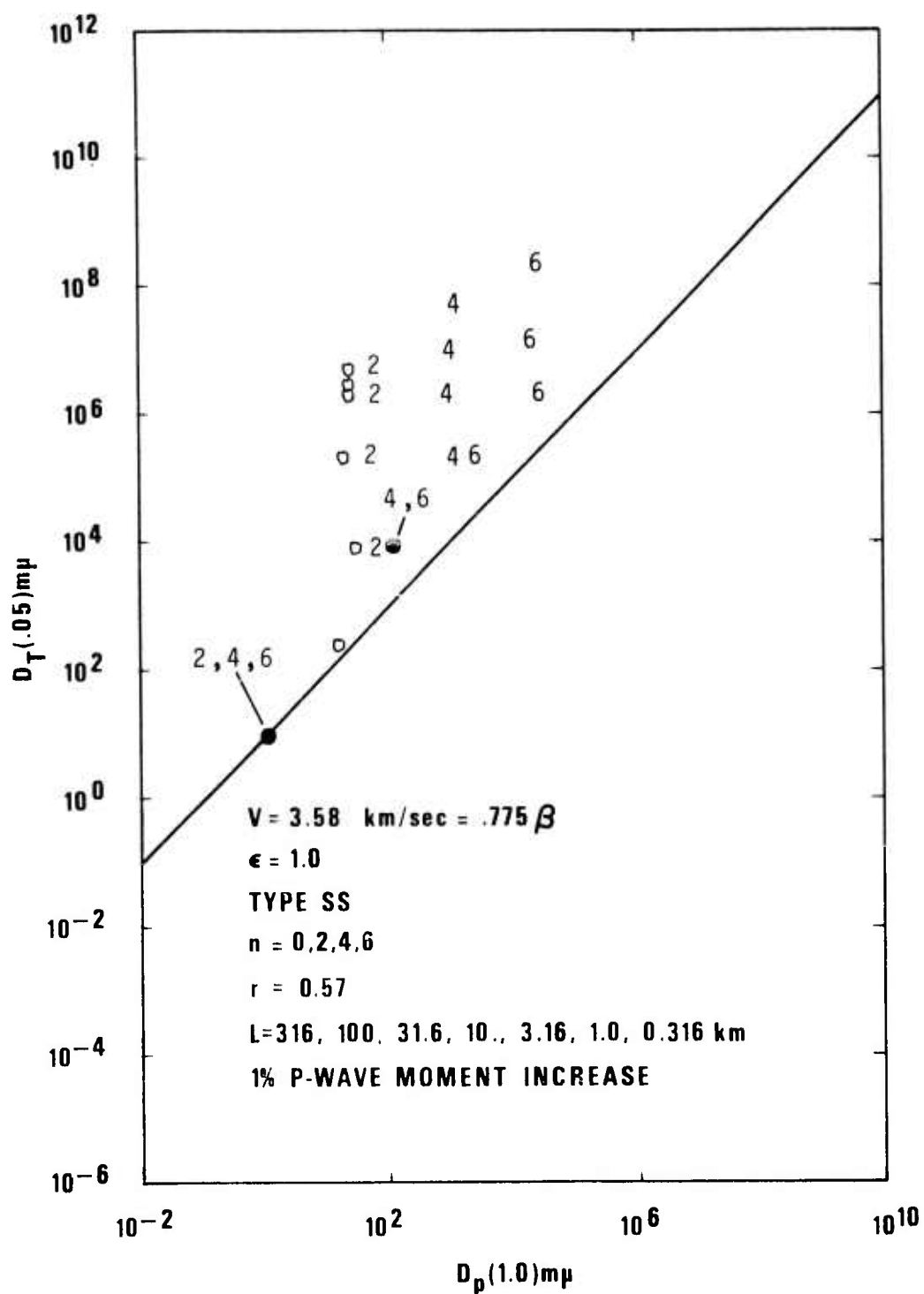


Figure 22. 20-second total displacement versus 1-second compressional displacement for simple earthquakes for a range of lengths, plus 0, 2, 4 or 6 sublevels with constant total moment leading to an increase of 1%. Ratio of subearthquake lengths $r = 0.57$.

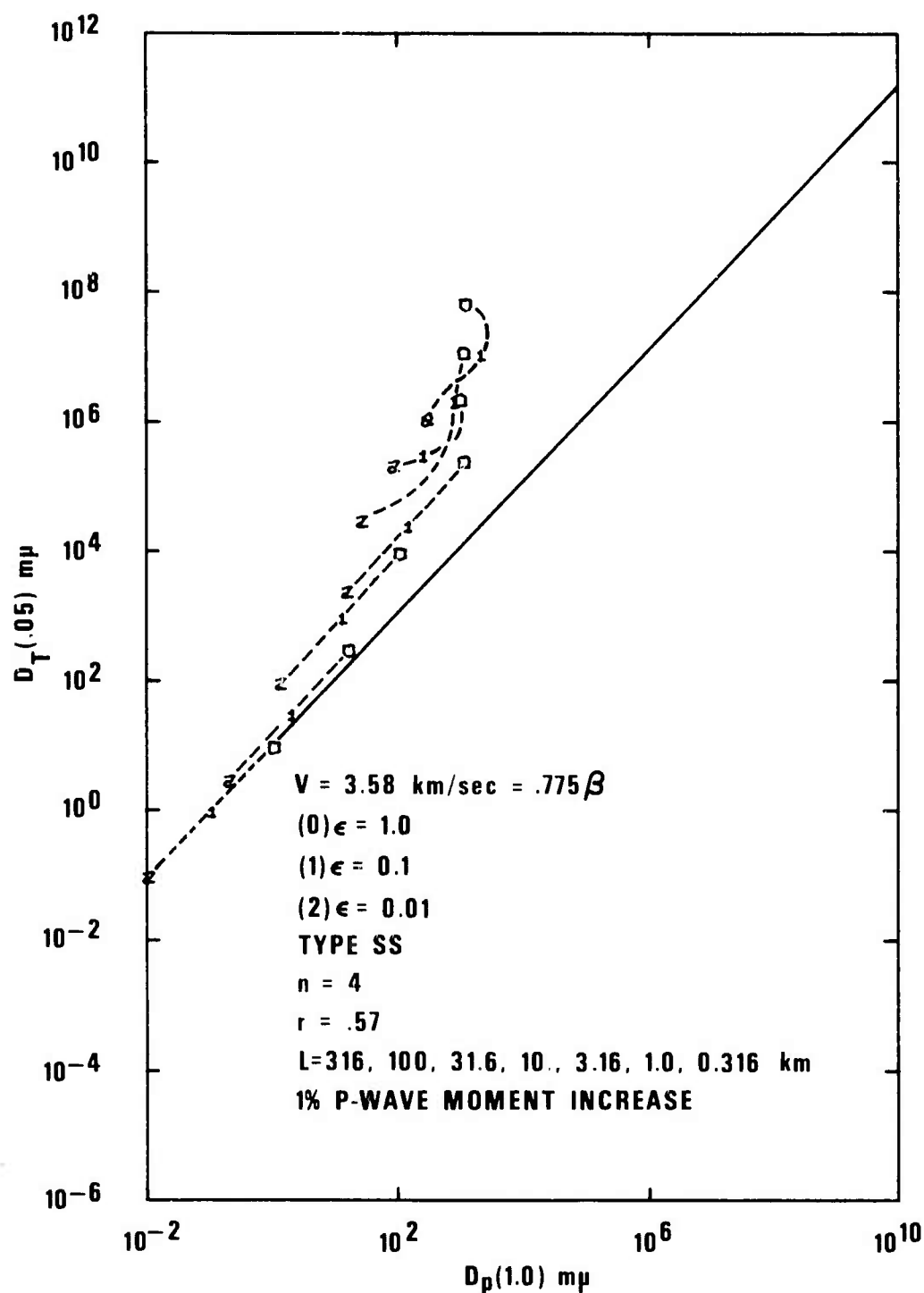


Figure 23. 20-second total displacement versus 1-second compressional displacement for simple earthquakes for a range of lengths, plus 4 sublevels with constant total moment leading to an increase of 1%. A range of fractional stress drops is presented, successive points are connected by dashed lines.

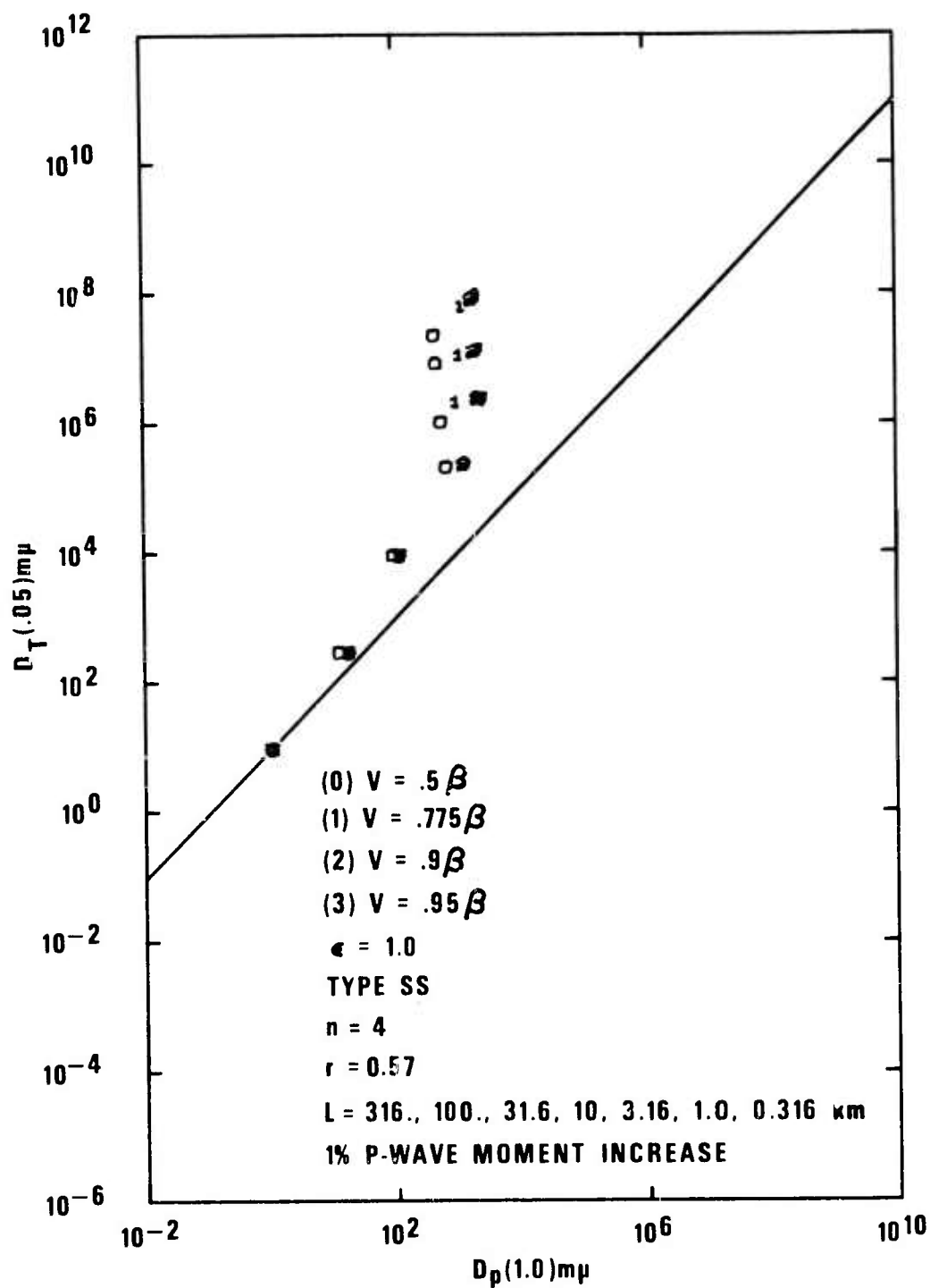


Figure 24. 20-second total displacement versus 1-second compressional displacement for simple earthquakes for a range of lengths, plus 4 sublevels with constant total moment leading to an increase of 1%. A range of propagation velocities is seen to affect the plot substantially less than does a range of subearthquake levels.

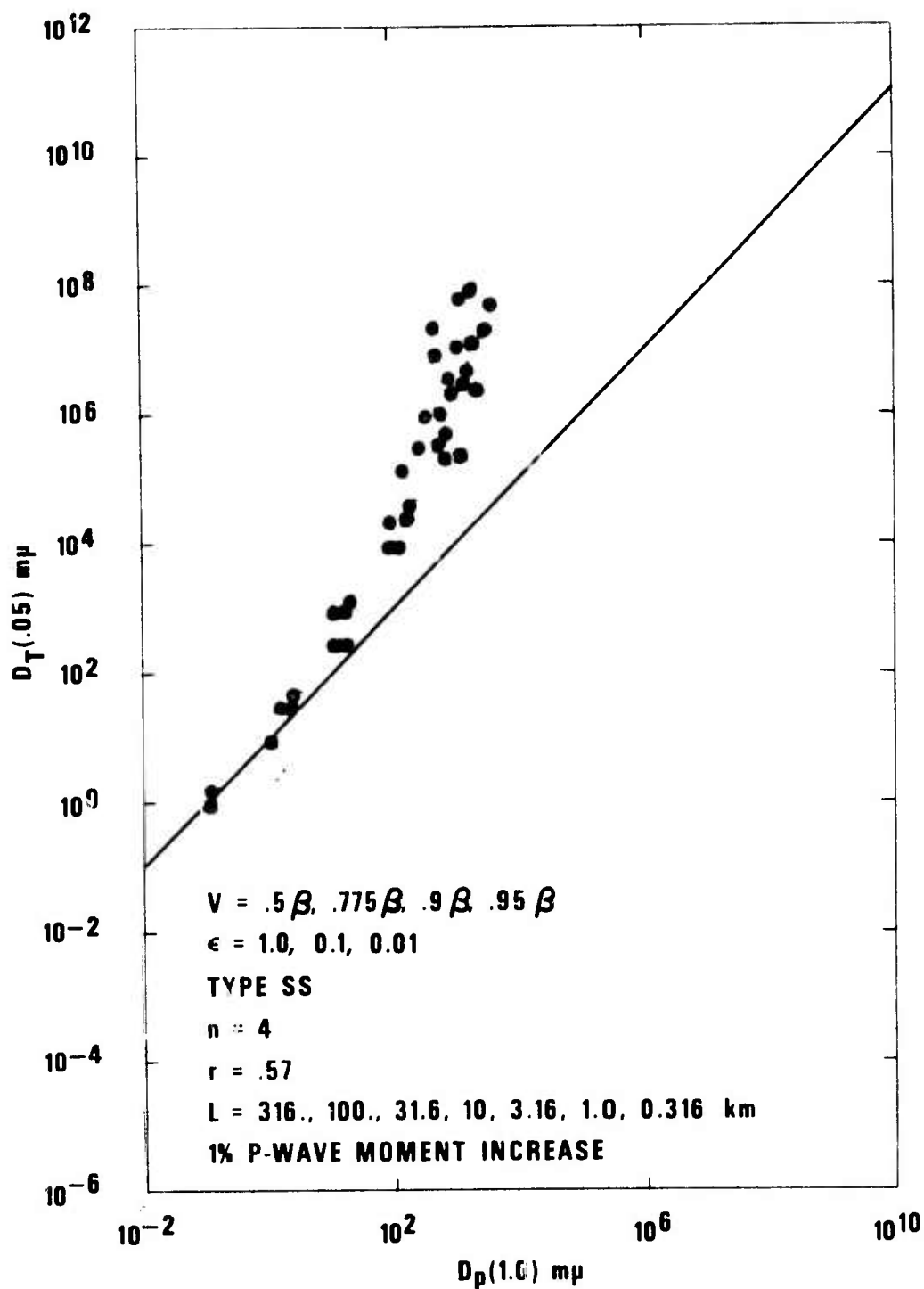


Figure 25. 20-second total displacement versus 1-second compressional displacement for simple earthquakes for a range of lengths, plus 4 sublevels with a constant total moment leading to an increase of 1%. The effects of a range in fractional stress drop and propagation velocity can be seen.

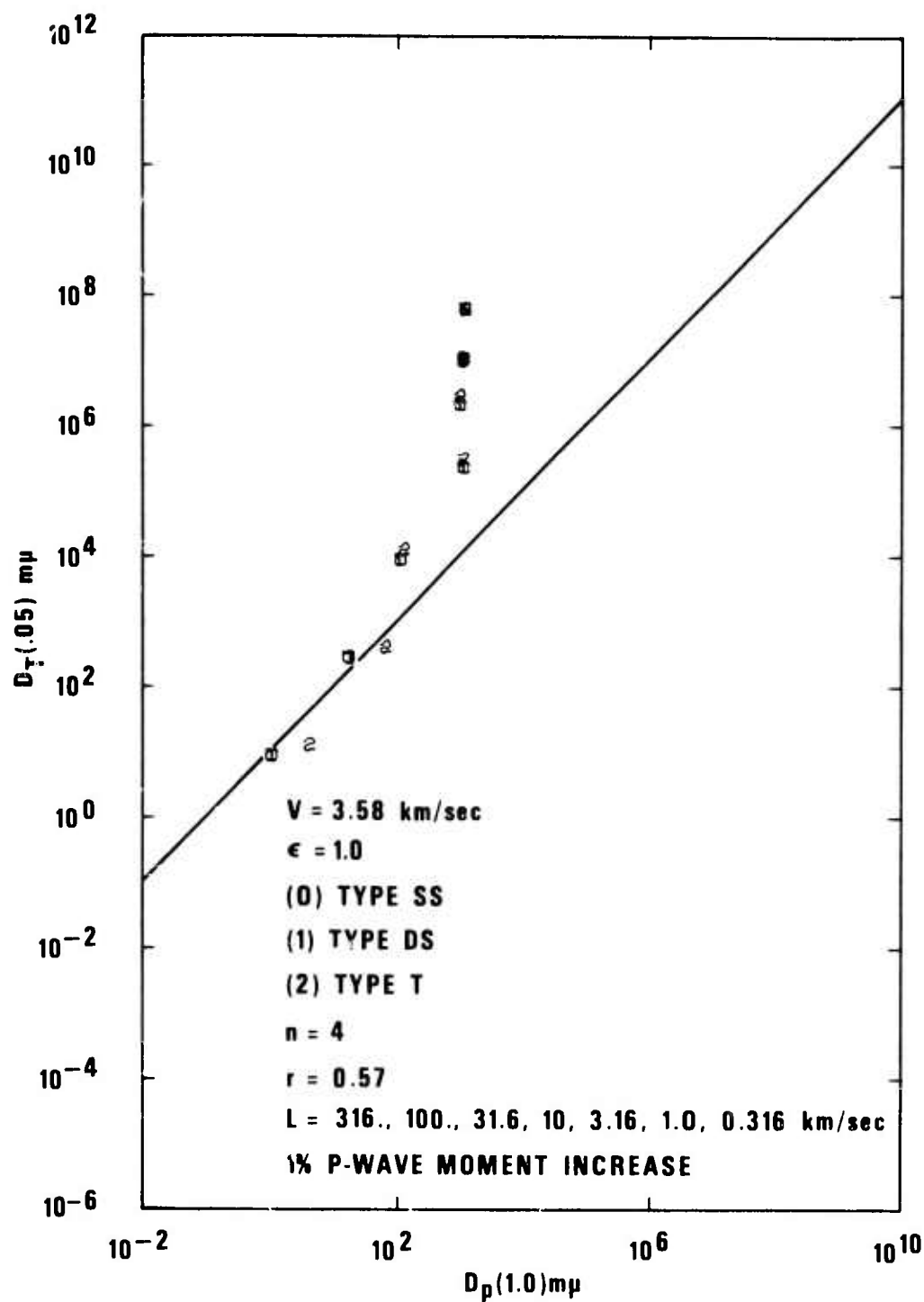


Figure 26. 20-second total displacement versus 1-second compressional displacement for simple earthquakes for a range of lengths, plus 4 sublevels with constant total moment leading to an increase of 1%. The effects of variation in the type of the simple earthquake can be seen to be relatively minor except earthquakes already near the limiting line.

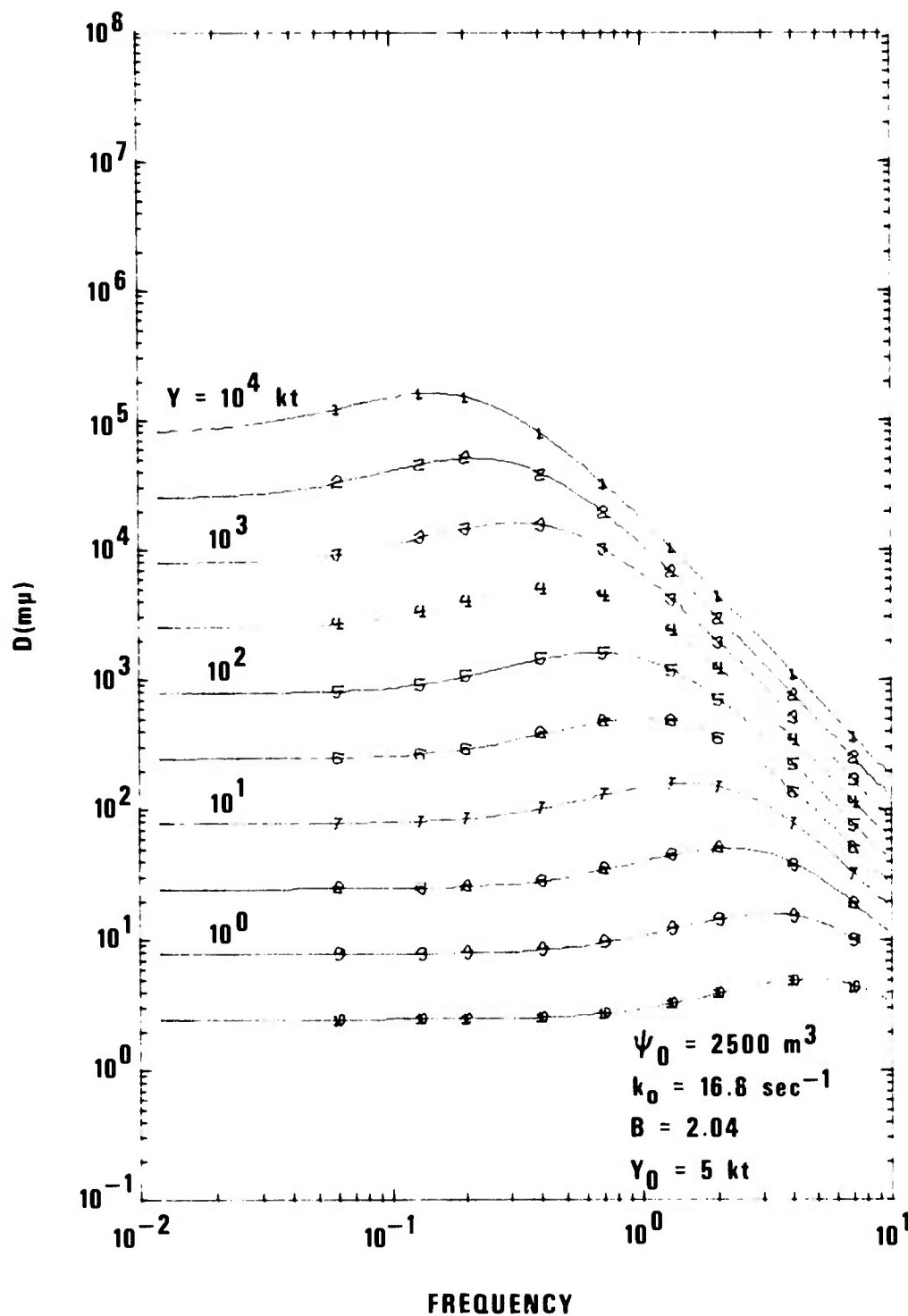


Figure 27. Displacement amplitude spectra for explosions in granite using the data of Werth and Herbst (1963) and the formulas of von Seggern and Blandford (1972).

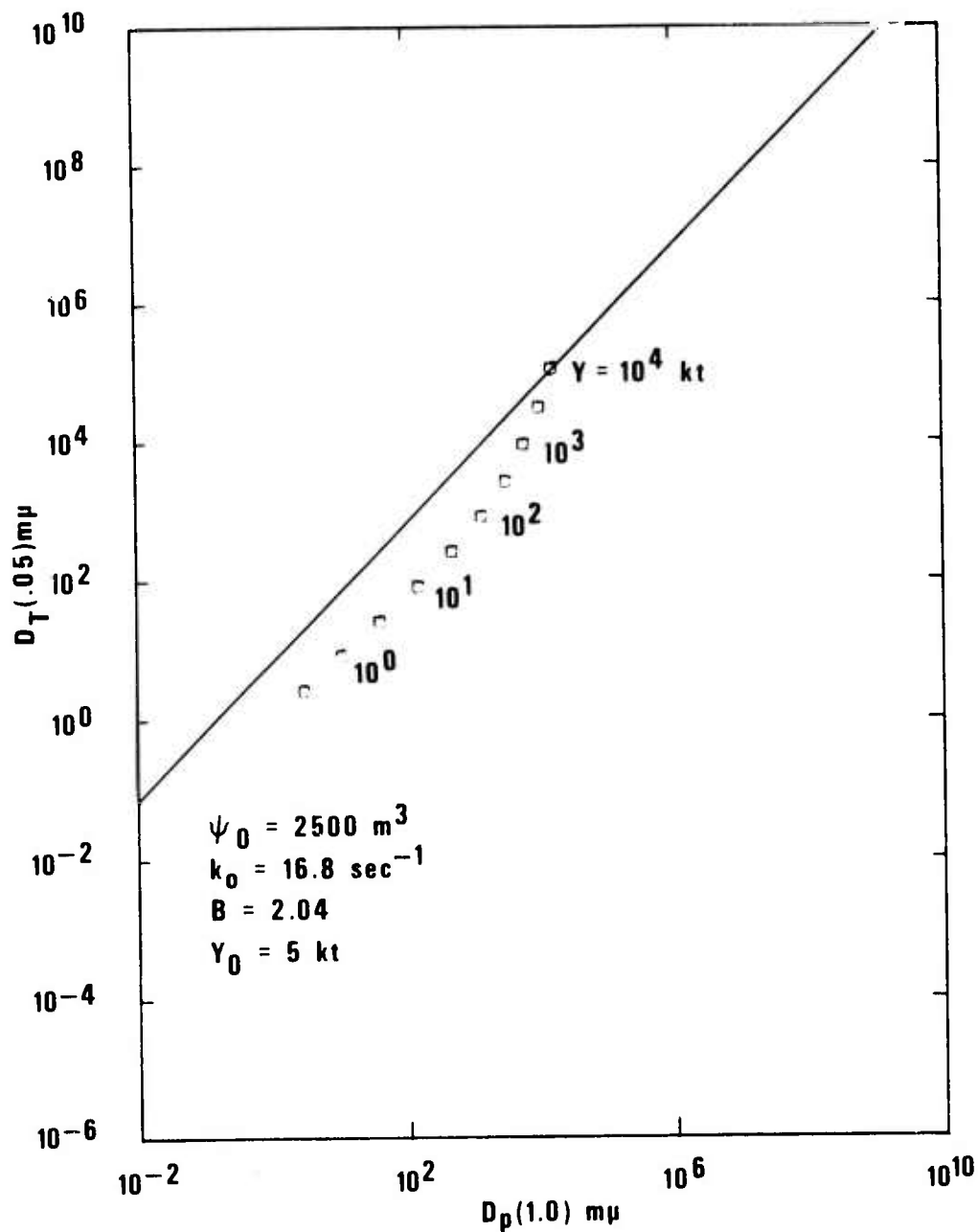


Figure 28. 20-second displacement versus 1-second displacement for explosions in granite using the data of Werth and Herbst (1963) and the formulas of von Seggern and Blandford (1973), for a range of yields.

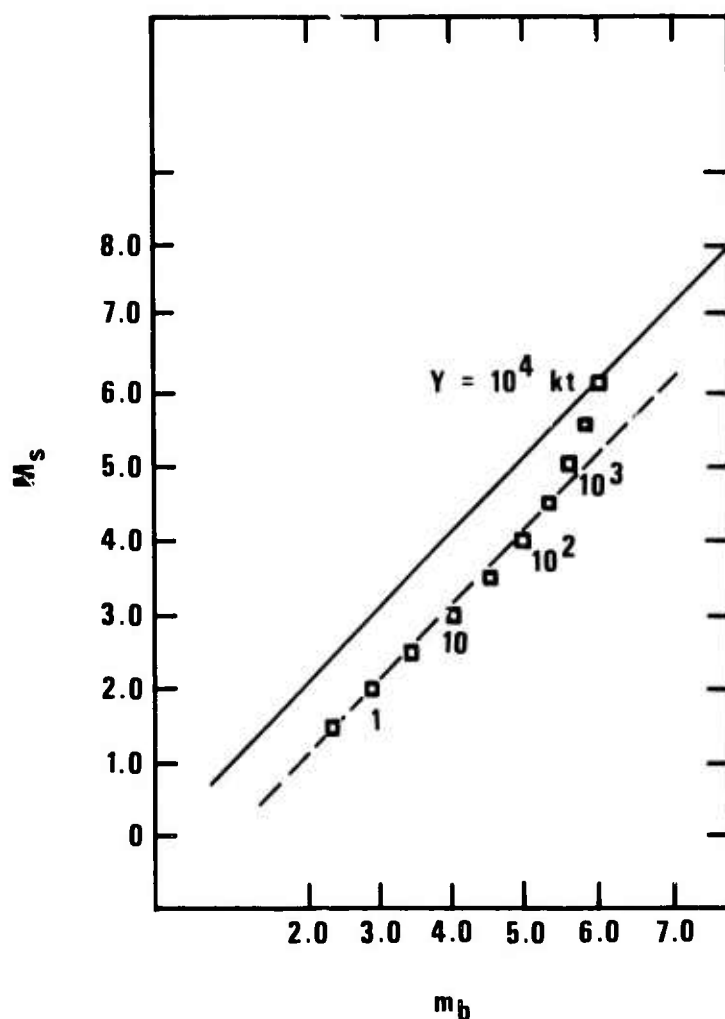


Figure 29. 20-second displacement versus 1-second displacement for explosions in granite using the data of Werth and Herbst (1963) and the formulas of von Seggern and Blandford (1973), for a range of yields. Figure has been calibrated to M_s and m_b values by use of solution for 100 kt explosion given by Douglas et al. (1973). Limiting earthquake line has also been drawn in.

Seismic signals at teleseismic distances

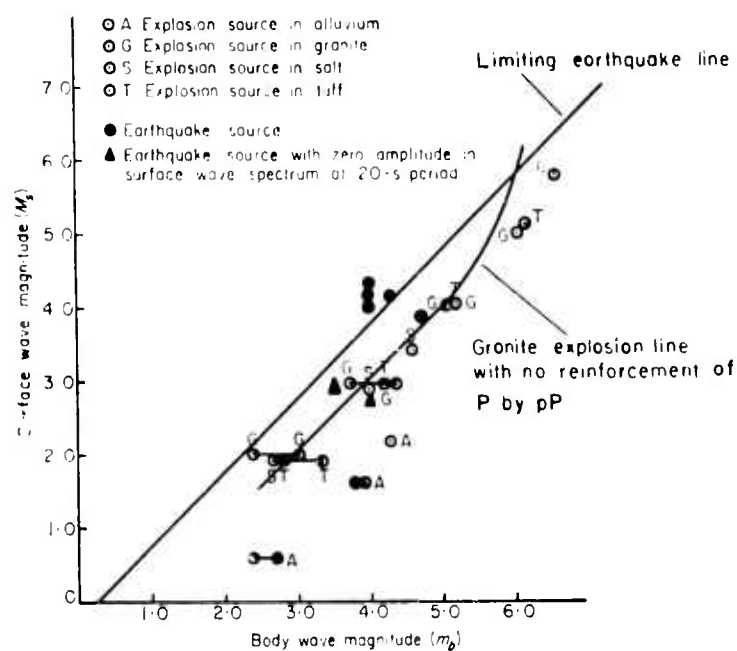


Figure 30. $M_S:m_b$ plot from Douglas et al. (1973) (see Table 2), together with the granite explosion line from Figure 29, and the limiting earthquake line.

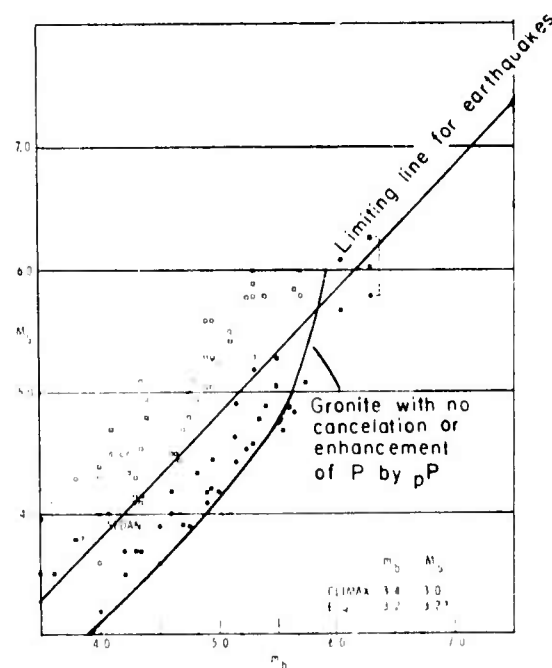


Figure 31. $M_S:m_b$ for U. S. earthquakes and explosions. Open symbols are earthquakes, closed symbols are explosions. From Evernden et al. (1971). Granite explosion line and limiting earthquake line have been drawn onto the original figure.

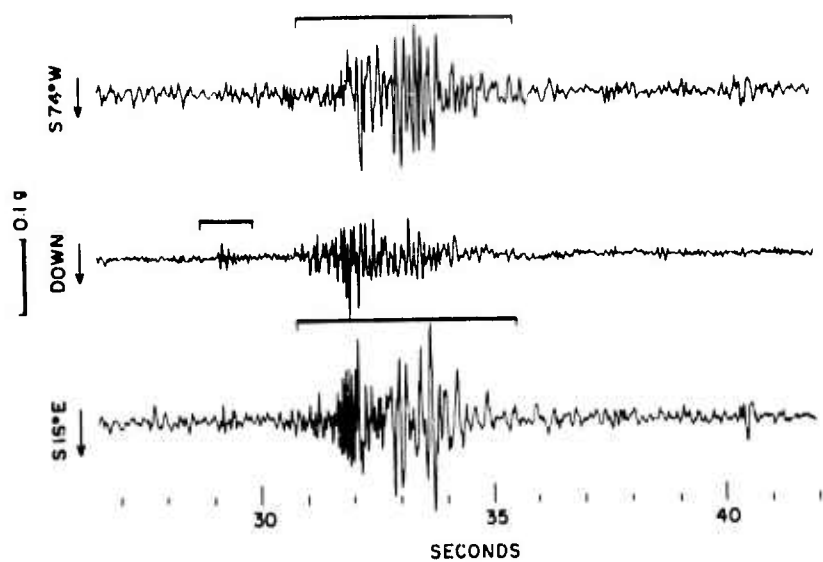


Figure 32a. Pacoima Dam accelerogram of event 1.

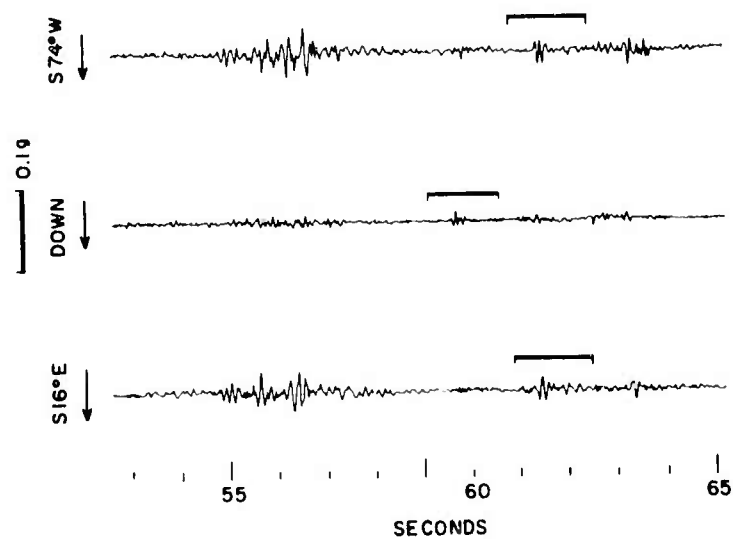


Figure 32b. Pacoima Dam accelerogram of events 2 and 3.

Figure 32. Pacoima Dam accelerograms of San Fernando aftershocks.

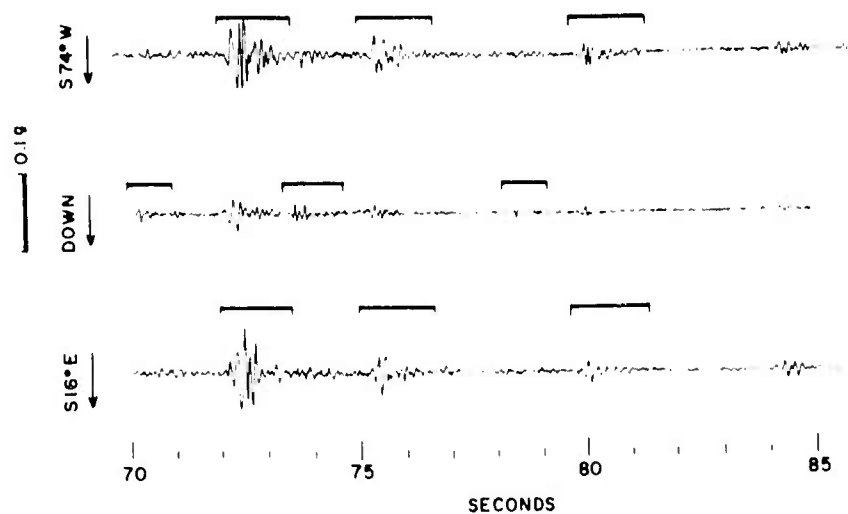


Figure 32c. Pacoima Dam accelerogram of events 4 to 7.

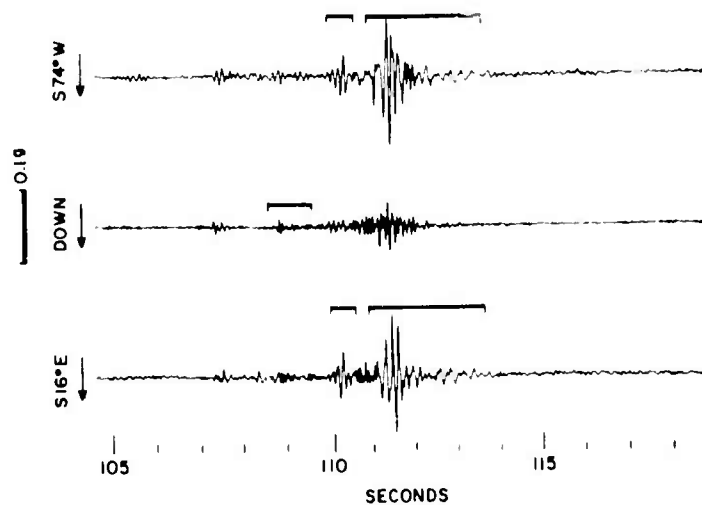


Figure 32d. Pacoima Dam accelerogram of events 8 to 10.

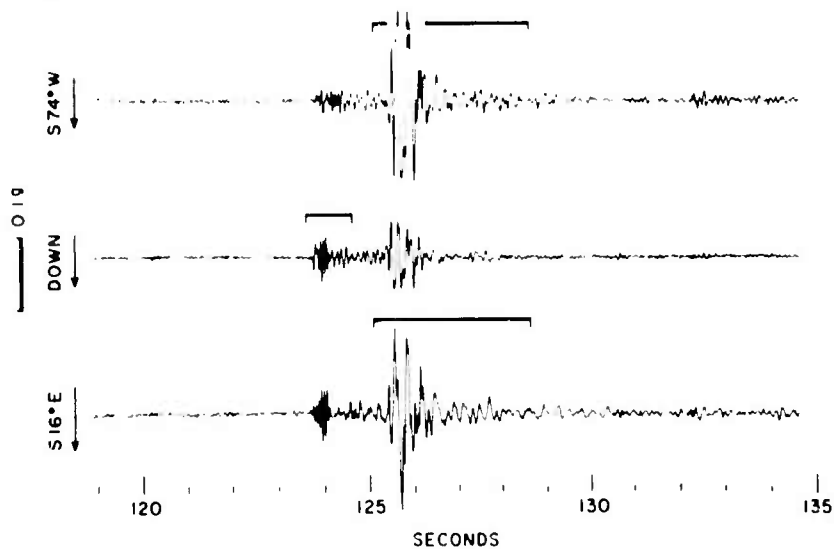


Figure 32e. Pacoima Dam accelerogram of event 11.

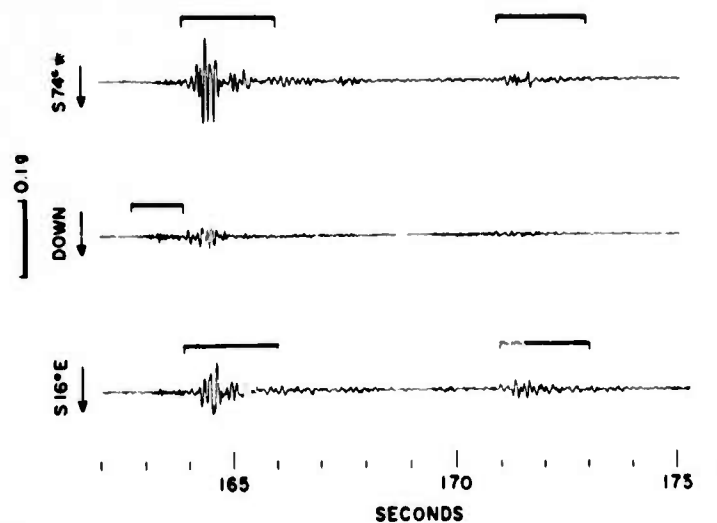


Figure 32f. Pacoima Dam accelerogram of events 16 and 17.

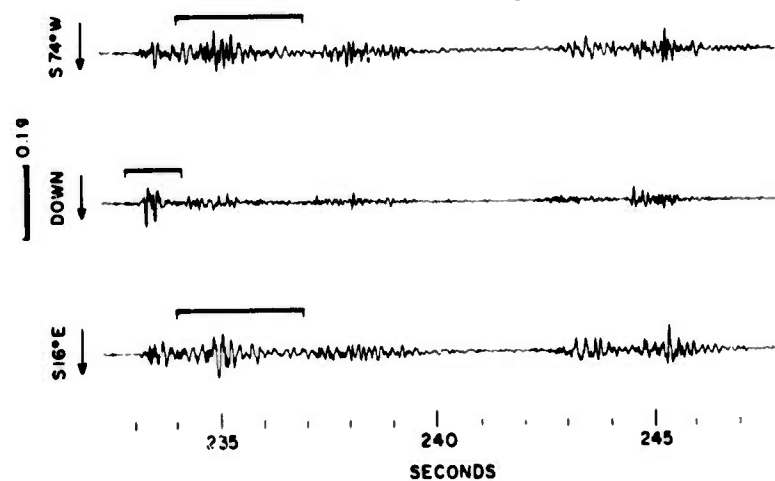


Figure 32g. Pacoima Dam accelerogram of events 22 to 25.

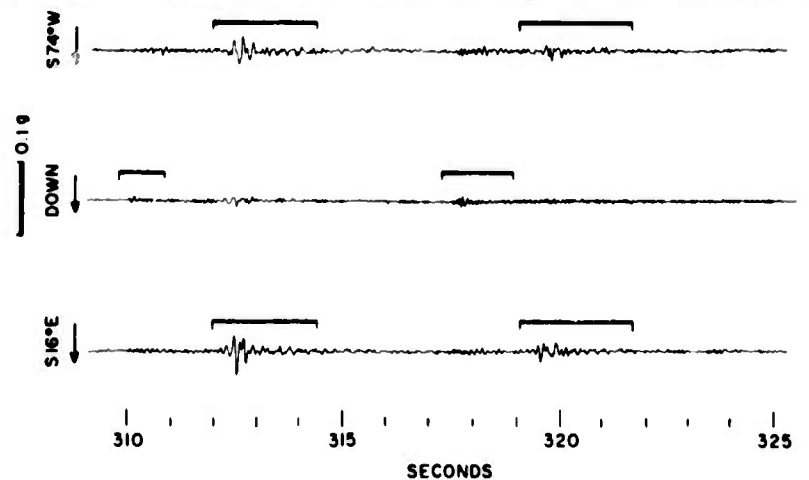


Figure 32h. Pacoima Dam accelerogram of events 30 and 31.

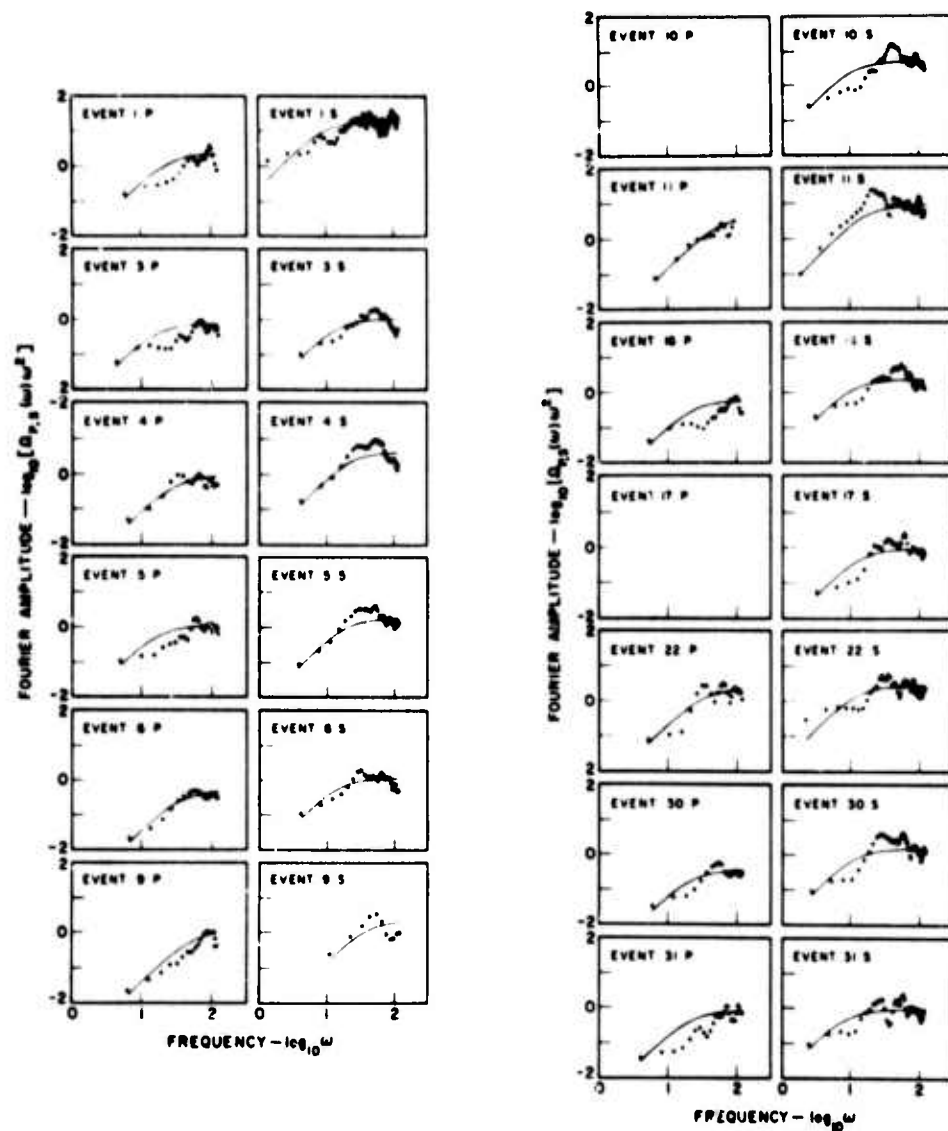


Figure 33. Fourier amplitude spectra of ground acceleration at the Pacoima Dam site for 13 aftershocks. From Trifunac (1972). The dots are the calculated and corrected average spectra. Full lines are Trifunac's theoretical spectra.

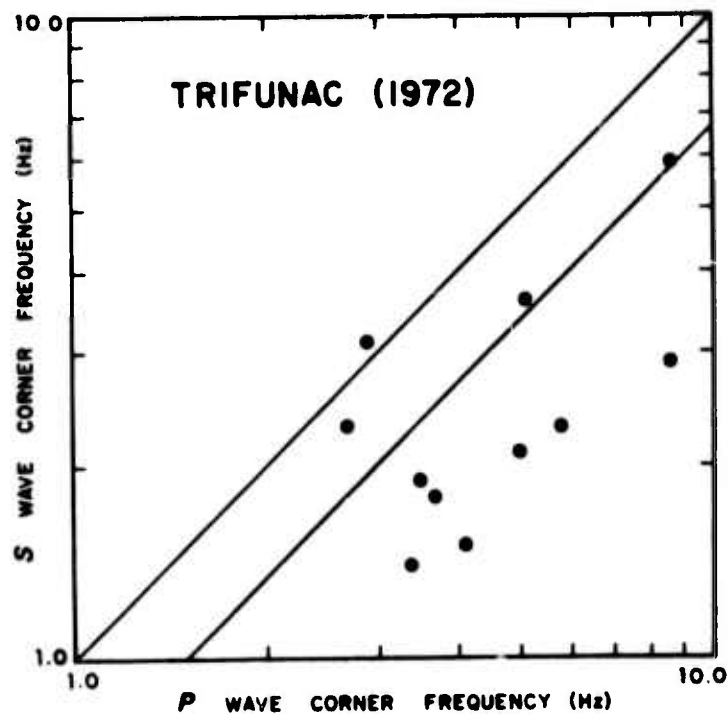


Figure 34. P wave corner frequencies versus S wave corner frequencies for large aftershocks of the 1971 San Fernando earthquake by the strong-motion instrument at Pacoima Dam. From Molnar et al. (1973) using data from Trifunac (1972).

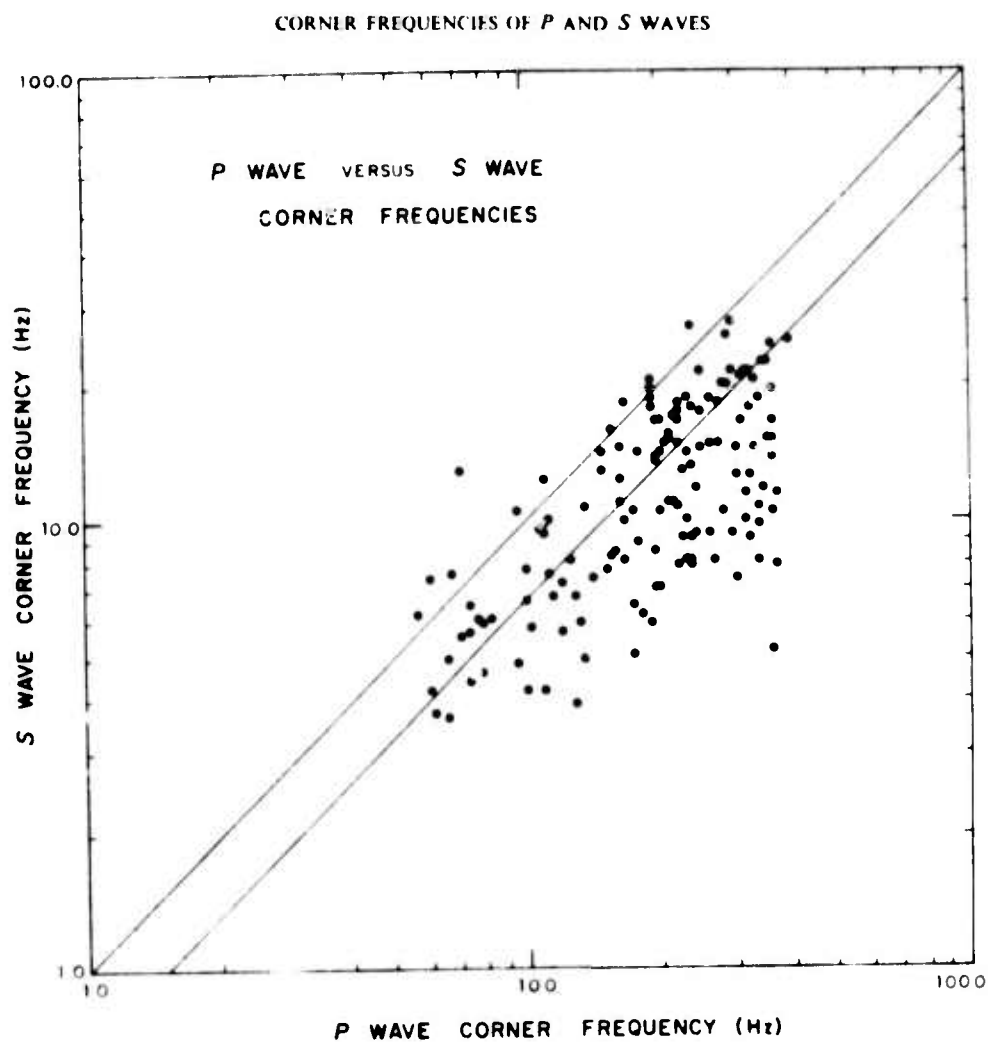


Figure 35. P wave corner frequencies versus S wave corner frequencies for earthquakes studied by Molnar et al. (1973).

